

Quantum-grade nanodiamonds for ultrabright spin detection in live cells

Keisuke Oshimi,¹ Hiromu Nakashima,¹ Sara Mandić,¹ Hina Kobayashi,¹ Minori Teramoto,² Hirokazu Tsuji,² Yoshiki Nishibayashi,² Yutaka Shikano,^{3,4,5} Toshu An,⁶ and Masazumi Fujiwara^{1,*}

¹*Department of Chemistry, Graduate School of Life, Environmental, Natural Science and Technology, Okayama University, Okayama 700-8530, Japan*

²*Advanced Materials Laboratory, Sumitomo Electric Industries, Ltd., Hyogo 664-0016, Japan*

³*Institute of Systems and Information Engineering, University of Tsukuba, Tsukuba, Ibaraki 305-8573, Japan*

⁴*Center for Artificial Intelligence Research (C-AIR), University of Tsukuba, Tsukuba, Ibaraki 305-8577, Japan*

⁵*Institute for Quantum Studies, Chapman University, Orange, CA 92866, USA*

⁶*School of Materials Science, Japan Advanced Institute of Science and Technology, Nomi, Ishikawa 923-1292, Japan*

Optically accessible spin-active nanomaterials are promising as quantum nanosensors for probing biological samples. However, achieving bioimaging-level brightness and high-quality spin properties for these materials is challenging and hinders their application in quantum biosensing. Here, we demonstrate ultrabright fluorescent nanodiamonds (NDs) containing 0.6–1.3-ppm nitrogen-vacancy (NV) centers by spin-environment engineering via enriching spin-less ¹²C-carbon isotopes and reducing substitutional nitrogen spin impurities. The NDs, readily introduced into cultured cells, exhibited substantially narrow optically detected magnetic resonance (ODMR) spectra, requiring 16-times less microwave excitation power to give an ODMR depth comparable to that of conventional type-Ib NDs. They show average spin-relaxation times of $T_1 = 0.68$ ms and $T_2 = 1.6$ μ s (1.6 ms and 2.7 μ s maximum) that were 5- and 11-fold longer than those of type-Ib, respectively. The bulk-like NV spin properties and bright fluorescence demonstrated in this study significantly improve the sensitivity of ND-based quantum sensors for biological applications.

INTRODUCTION

Engineering spin-active materials is critical to developing highly sensitive quantum nanosensors, as demonstrated by nanodiamonds (NDs) containing color defect centers [1, 2], organic nanosolids with radical molecules [3], rare earth nanocrystals [4], and nanoflakes of hexagonal boron nitrides [5, 6]. Among these spin-active materials, NDs containing nitrogen-vacancy (NV) centers are the most advanced quantum nanosensors utilized for biological applications owing to their multimodal sensing capability [7, 8], photostability [9], chemical functionality [10], and biocompatibility [11]. The NV quantum nanosensors exploit the dependence of optically accessible NV electron spins on magnetic field, electric field, and temperature of the surrounding cellular environment [12], which enables sub-cellular measurements of either those values or extended physicochemical parameters, such as pH [13, 14], magnetic ions [15, 16], reactive oxygen species [17, 18] and rheology [19, 20]. In the majority of the cases, these sensing modalities measure the frequency shift (or modulated relaxation times) in optically detected magnetic resonance (ODMR) of NV centers. Therefore, measurement sensitivity is critically dependent on the quality of the NV spin properties [21].

However, current fluorescent NDs incorporating high-density NVs that show bioimaging-level brightness exhibit deficient spin qualities in contrast to bulk diamonds.

They show broad ODMR spectra and short spin relaxation times, which substantially deteriorates the measurement sensitivity [21, 22]. The NV spins are affected by (i) a high concentration of spin impurities and (ii) surface spin noise [23–25]. However, recent studies suggest that the effects of these factors on NDs might be mitigated. First, high-quality synthetic bulk diamonds with dense NV ensembles have realized high-yield NV production while enriching spinless ¹²C-carbon isotopes and reducing substitutional nitrogen impurity for quantum sensor applications [26–29]. These bulk diamonds exhibited high NV spin qualities and demonstrated fascinating applications, including nanoscale nuclear magnetic resonance [30, 31] and neural monitoring [7, 32]. Second, previous studies revealed that the surface spin noises reduced the NV spin relaxation time in NDs with d^{-4} scaling for the ND diameter (d) [33]. The spin deterioration of NVs is prominent only for $d < 80$ nm, and this surface effect might not be predominant for a majority of the NDs used in the quantum biological applications owing to their relatively large diameter ($d > 80$ nm) [1, 2, 19, 34], which is corroborated by observation of single-NV NDs with long spin coherence, wherein the spin impurities could be minimized to ppb level for quantum applications requiring single NVs [24, 35].

Here, we demonstrate NDs possessing bulk-like NV spin properties by controlling the spin impurities of ¹³C and N, while increasing the NV concentration for bioimaging-level brightness. The spin relaxation times of the NVs, i.e., T_1 and T_2 , in these spin-controlled NDs are enhanced by a factor of 5 for T_1 and 10 for T_2 , com-

* masazumi@okayama-u.ac.jp

pared with conventional type-Ib NDs. The results indicate the possibility of realizing quantum-grade NDs that can implement various quantum-enhanced measurement protocols for biological samples and applications.

RESULTS

To achieve a high NV concentration exhibiting bioimaging-level brightness with simultaneous reduction in the amount of spin impurities, we use NV-enriched single-crystalline bulk diamonds, wherein the major spin impurities of N (the so-called P_1 center) and ^{13}C are minimized (Fig. 1a). We prepared NDs via pulverization of single-crystalline bulk diamonds grown using a high-pressure high-temperature (HPHT) method with controlled impurities of $[^{12}\text{C}] = 99.99\%$ and $[\text{N}] = 30\text{--}60$ ppm (see Methods). These NDs (hereafter called ^{12}C , N-NDs) exhibit NV red fluorescence under green optical excitation with ODMR signal upon microwave irradiation (Fig. 1b). To characterize the fluorescence brightness and size, the NDs were suspended in water and drop-casted onto coverslips with engraved island grids (Fig. 1c). We performed single-particle characterization using confocal fluorescence and atomic force microscopy (AFM). Figure 1d shows the topography and corresponding confocal fluorescence images of the area containing several ^{12}C , N-NDs. We observe bright fluorescence emission from these NDs (with a photon-count rate of 1500 kcps) at an optical excitation intensity of $\sim 7\text{ kW cm}^{-2}$. Their mean fluorescence intensity is comparable to the type-Ib NDs, sufficient for bioimaging (Supplementary Figs. S1a–d). A close view of the ND topography indicated by the white arrow is shown in Fig 1e, where the size is determined to be $h = 180$ nm by taking the height of the sample from the xy-imaging plane. Further, Fig. 1f shows the typical fluorescence spectra with zero phonon line at 637 nm, confirming that the fluorescence of the ^{12}C , N-NDs primarily originates from the negatively charged NVs.

The concentration of NV in NDs is typically determined by electron paramagnetic resonance (EPR) spectroscopy [36]. However, this method requires hundreds of milligram of samples and cannot be employed for the present NDs due to the small amount. Alternatively, we determined $[\text{NV}]$ of the NDs by measuring their size and fluorescence intensity and comparing them with those of two types of type-Ib NDs having mean sizes of 100 nm (Ib-100) and 600 nm (Ib-600) (Figs. 1g, h). The size analysis revealed the ND mean sizes as 98.5, 485, and 277 nm for the Ib-100, Ib-600, and ^{12}C , N-NDs, respectively (Fig. 1g). These mean sizes, which were relatively smaller than the supplier’s specification, reflected the typical disk-like ND morphology [37], which was more prominent in Ib-600. Because the number of NVs is proportional to the volume of NDs, we assume that the fluorescence intensity is proportional to

the ND volume: $I \propto [\text{NV}]V$, where I and V are the fluorescence photon-count rate and volume of the NDs, respectively. To determine $[\text{NV}]$ of the ^{12}C , N-NDs from $[\text{NV}]$ of Ib-100 (Ib-600), we used the relationship: $[\text{NV}]_{12\text{C},\text{N}} = I_{12\text{C},\text{N}} I_{\text{Ib}100}^{-1} V_{\text{Ib}100} V_{12\text{C},\text{N}}^{-1} [\text{NV}]_{\text{Ib}100}$ ($I_{12\text{C},\text{N}} I_{\text{Ib}600}^{-1} V_{\text{Ib}600} V_{12\text{C},\text{N}}^{-1} [\text{NV}]_{\text{Ib}600}$). $[\text{NV}]$ of the ^{12}C , N-NDs was 0.6–1.3 ppm, which was determined based on $[\text{NV}] \approx 3$ and 3.5 ppm for the Ib-100 and for Ib-600 NDs, respectively; these $[\text{NV}]$ values of the Ib-100 and for Ib-600 NDs were adopted from the specification sheet and were considered based on the conceivable ND morphology in terms of the aspect ratio of the NDs (see Supplementary Information for the details).

Next, we characterized the NV electron spin properties of the ^{12}C , N-NDs by measuring their continuous-wave (CW) ODMR spectra. Quantitative characterization of the CW-ODMR spectra over different NDs requires a well-defined spatial microwave-excitation-field pattern because the CW-ODMR spectral shape is sensitive to the applied microwave intensity. Therefore, we exploited an on-chip platform based on a previously developed notch-shaped antenna pattern [38], which provided a uniform distribution of the microwave magnetic field ($|\mathbf{B}|$) that was quantitatively defined at each grid (Figs. 2a, b).

In this experiment, we selected the second nearest grid ($x = 0.2$ mm) from the edge of the central waveguide ($x = 0.0$ mm), where the variation in $|\mathbf{B}|$ was only 0.02 G for the microwave power of 26.1 mW (14.2 dBm) utilized in the CW-ODMR experiments, as shown in Figs. 2b, c (see Table S1). This variation resulted in only a 0.8% difference in the ODMR depth and a 10% change in the Rabi-frequency period, which enabled the characterization of the NV spins at the same microwave power without requiring Rabi frequency measurement for each ND. To observe the ODMR differences among the Ib-100, Ib-600, and ^{12}C , N-NDs, the microwave power required to attain a 3% ODMR contrast was determined for each type of these NDs at the same optical intensity. The ^{12}C , N-NDs exhibited a 3% ODMR contrast with a microwave power of 1.04 mW in the detection area ($|\mathbf{B}| = 0.041$ G in the grid position), whereas the Ib-100 and Ib-600 NDs required 10.4 mW ($|\mathbf{B}| = 0.13$ G) and 20.7 mW ($|\mathbf{B}| = 0.18$ G) to obtain a 3% contrast (top panel in Fig. 2d). This result indicates that to attain the same 3% ODMR contrast, the microwave power required by the ^{12}C , N-NDs is 10 and 20 times lower than those required by the Ib-100 and Ib-600 NDs, respectively. Moreover, the ODMR spectra of the ^{12}C , N-NDs were substantially narrower than those of the type-Ib NDs. We determined the spectral evolution of all the NDs under an applied microwave power of 26.1 mW (bottom panel in Fig. 2d). The ODMR contrast shown by the ^{12}C , N-NDs was considerably deeper than those shown by the Ib-100 and Ib-600 NDs, and this result confirmed the improve-

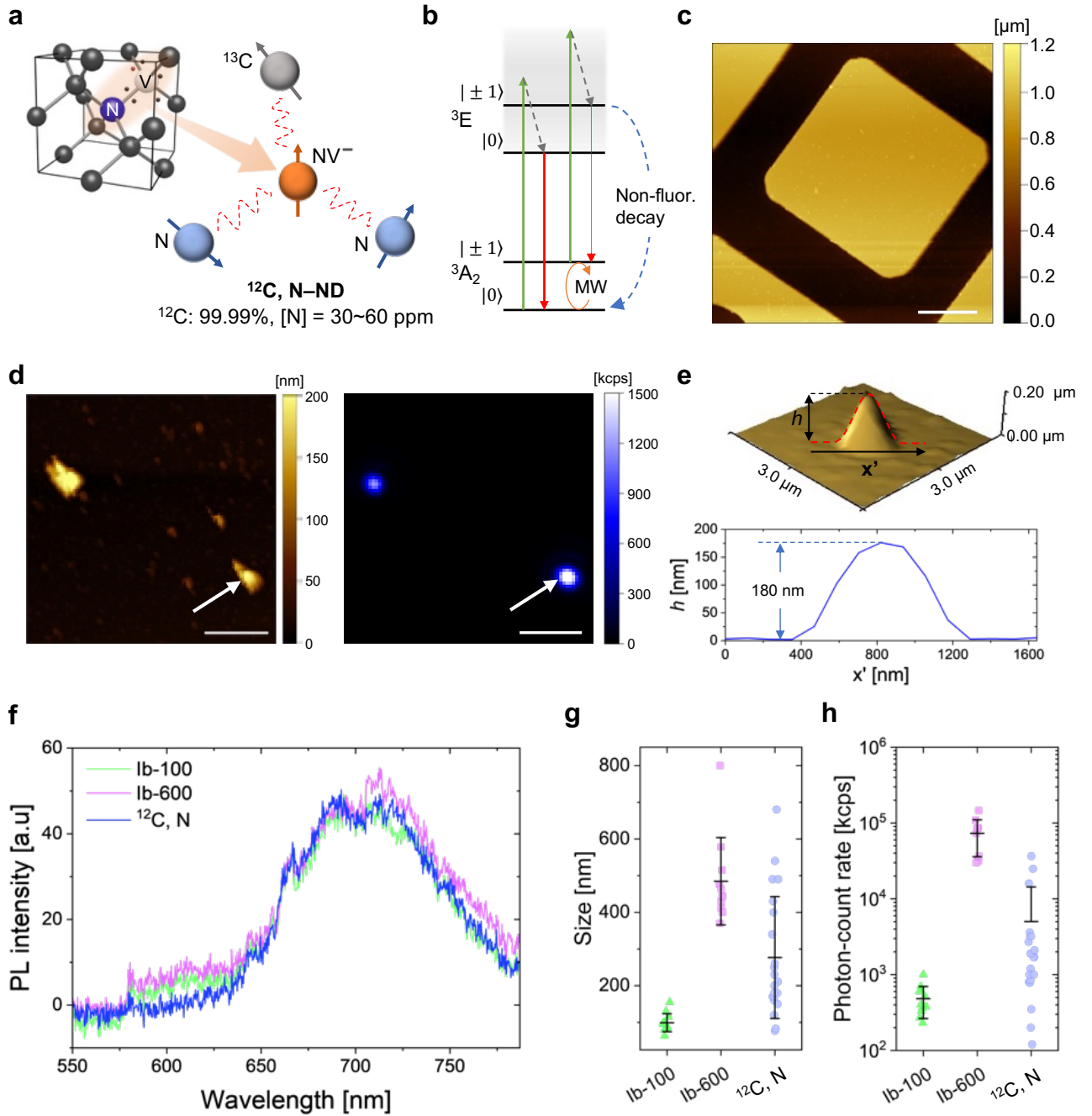


FIG. 1. (a) Illustrations of the NV crystal structure and the interaction of NV with the spin bath of N and ^{13}C . (b) Schematic representation of simplified energy level structure of NV centers. $|0\rangle$ and $|\pm 1\rangle$ are the spin sublevels for $m_s = 0$ and $m_s = \pm 1$, respectively. MW: microwave. ${}^3\text{A}_2$ (${}^3\text{E}$): triplet ground (excited) state. (c) AFM topography image of a single grid engraved on a coverslip. Scale bar: $10\ \mu\text{m}$. (d) AFM topography and the corresponding confocal fluorescence images of ^{12}C , N-NDs on a grid. Scale bars: $2\ \mu\text{m}$. (e) Three-dimensional visualization of the topography of the ND indicated by the white arrow in Fig. 1(d) (top) with a cross-section along the x' axis (bottom). (f) Fluorescent spectra of type-Ib NDs and ^{12}C , N-NDs. (g) Statistical plots of the ND size determined by AFM and (h) photon-count rate at an optical excitation intensity of $\sim 7\ \text{kW cm}^{-2}$ for Ib-100, Ib-600, and ^{12}C , N-NDs. Mean and standard deviation (1σ) are indicated in the statistical plots. The error bar is shown only for the upper error side ($+\sigma$) for ^{12}C , N-NDs in Fig. 1(h), where a large standard deviation ($\sigma = 5000\ \text{kcps}$) makes a negative lower side ($-\sigma$) invisible in a log plot.

ment in the NV spin properties of the NDs developed in this study.

Subsequently, we performed a statistical analysis of the CW-ODMR spectra of these NDs (Figs. 2e–g). The re-

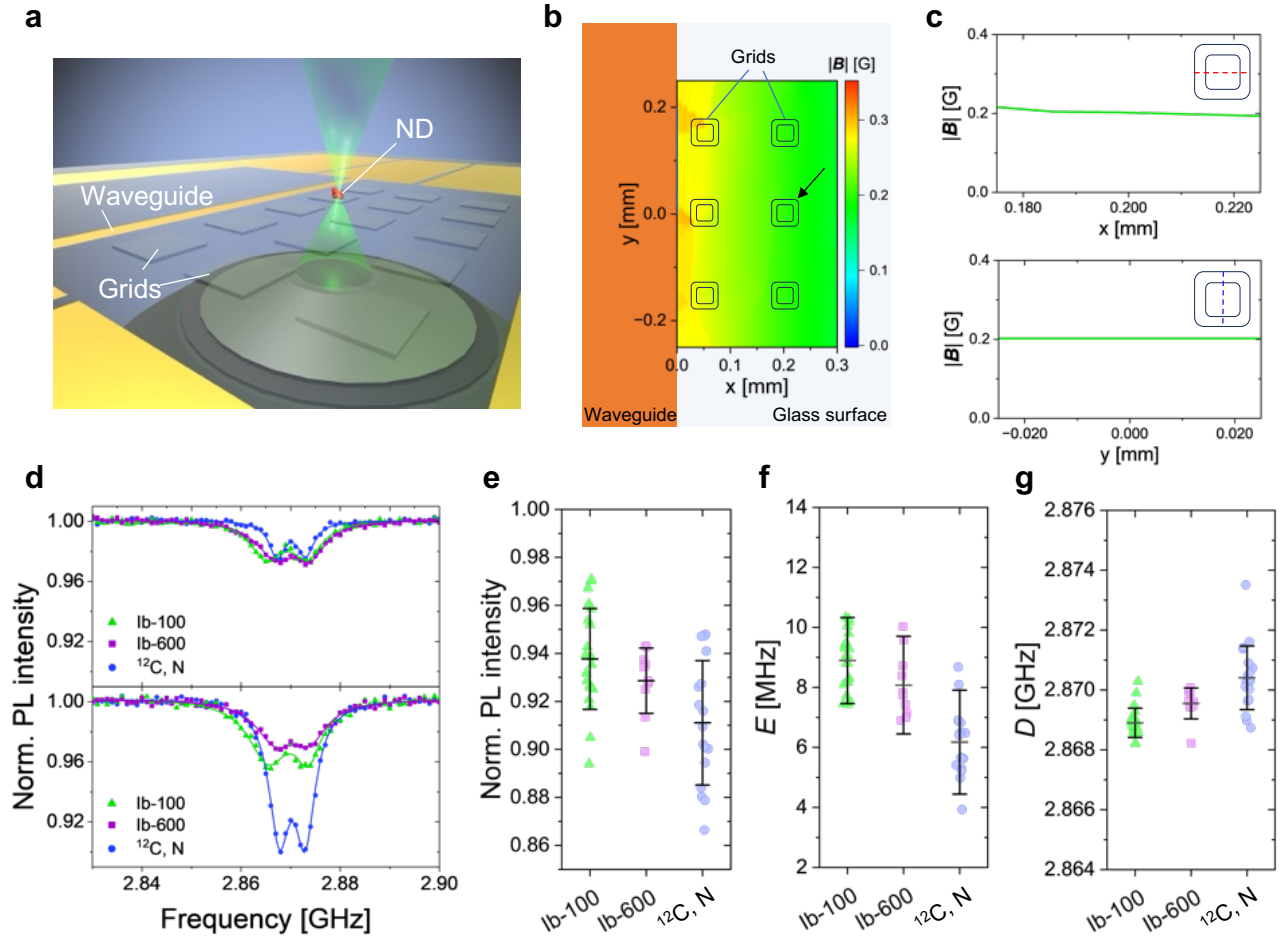


FIG. 2. (a) Schematic representation of NDs on grids of the notch-shaped microwave antenna. (b) Heat map of simulated magnetic field ($|\mathbf{B}|$) on the antenna overlaid with schematic grid structures. 26.1 mW microwave power was used for the simulation. (c) Cross-sections of $|\mathbf{B}|$ over the grid indicated by a white arrow at $(x, y) = (0.2, 0)$ mm along x (top) and y axes (bottom). (d) Representative CW-ODMR spectra of an Ib-100, Ib-600, and ^{12}C , N-ND when the microwave power was adjusted to give 3% ODMR contrast (top) and with the common microwave power of 26.1 mW at the input of the notch area (bottom). A common optical intensity was used in both the panels ($\sim 6 \text{ kW cm}^{-2}$). The lines are double-Lorentzian fits. Statistical plots for the Ib-100 (green triangle), Ib-600 (purple square), and ^{12}C , N-NDs (blue circle) for (e) ODMR depth, (f) E , and (g) D . Mean and standard deviation (1σ) are indicated in the statistical plots.

sults demonstrated that on average, the ODMR depth was greater for the ^{12}C , N-NDs than for the Ib-100 and Ib-600 counterparts (Fig. 2e). We further analyzed spectral parameters for peak splitting (E) related to crystal strains and zero-field splitting (D) to evaluate more NV intrinsic spin properties of the NDs (see Methods). The mean of E for the ^{12}C , N-NDs was smaller than that for the type-Ib NDs by 2–3 MHz (Fig. 2f), indicating reduced crystal strain in the ^{12}C , N-NDs. The effect of the geomagnetic field on E was insignificant due to the random NV quantization axes (see Supplementary Information). Unexpectedly, the mean D of the ^{12}C , N-NDs was 1–2 MHz higher than those of the type-Ib NDs (Fig. 2g). Because the mean D of Ib-600 was higher than that of Ib-100 as well, this increment in the mean D possibly results from the ND size difference among the ^{12}C , N-and

type-Ib NDs; however, the absolute value of D has not been studied in the context of ND size, and the exact origin of the increased D continues to remain unclear.

To further evaluate the NV spin properties of the ^{12}C , N-NDs, we performed pulsed ODMR experiments and determined the longitudinal (T_1) and transverse (T_2) relaxation times of the ^{12}C , N- and Ib-100 NDs (Figs. 3a–d). An external magnetic field was applied in a controlled orientation to split the spectra into two peaks (Fig. 3a). By addressing the lower-energy peak, we measured Rabi nutation to determine the duration of π -pulse used in the subsequent T_1 and T_2 measurements, where the typical duration of the π -pulse is 300–400 ns. (Fig. 3b). Figures 3c, d show the representative T_1 and T_2 profiles for the ^{12}C , N- and Ib-100. Both profiles exhibit a substantial extension of the relaxation times in the ^{12}C , N-NDs. T_1

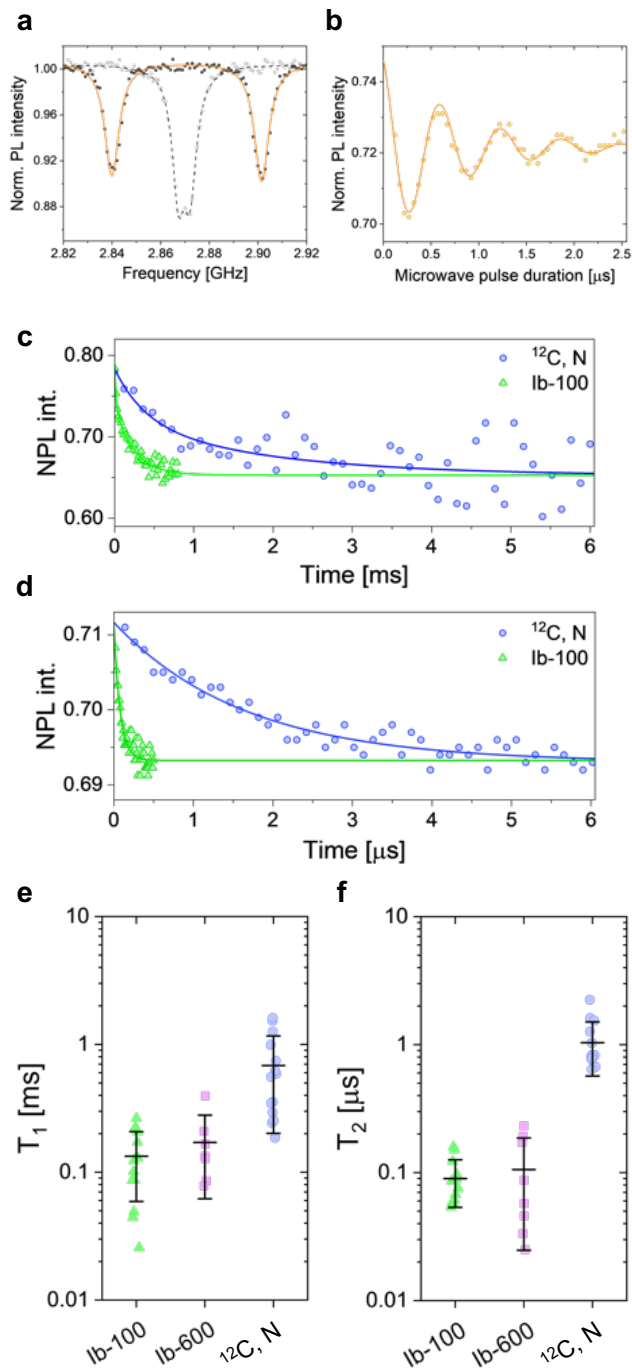


FIG. 3. (a) ODMR spectra and double-Lorentzian fits of a representative ^{12}C , N-ND with (black dots and orange solid line) and without (gray dots and gray dashed line) an external magnetic field. (b) A typical Rabi oscillation observed in the ^{12}C , N-NDs. A solid line is a sine-damp fit. Representative profiles of (c) all-optical T_1 relaxometry and (d) $\pi/2$ -spin echo measurements for the ^{12}C , N- and Ib-100 NDs. Statistical plots of T_1 (e) and T_2 (f) relaxation times for the ^{12}C , N-, Ib-100 and Ib-600 NDs.

profiles were fit with a biexponential decay, and T_2 profiles with a stretched exponential decay (see Methods).

We performed statistical analysis by measuring a number of NDs as shown in Figs. 3e, f. The ^{12}C , N-NDs exhibit $T_1^{\text{max}} = 1.6$ ms and $T_2^{\text{max}} = 2.7$ μs in maximum, which are close to the bulk-limited relaxation times for the present nitrogen concentration of 30–60 ppm ($T_1 \approx 3$ ms [39], $T_2 \approx 3$ –5 μs [28]). T_1 of the ^{12}C , N-NDs (0.68 ± 0.48 ms) is more than 4–5 times longer than those of the type-Ib NDs (Ib-100: 0.13 ± 0.07 ms, Ib-600: 0.17 ± 0.11 ms), and T_2 of the ^{12}C , N-NDs (1.6 ± 0.6 μs) is more than 11 times longer than those of the type-Ib NDs (Ib-100: 0.14 ± 0.05 μs , Ib-600: 0.11 ± 0.08 μs). These values represent a remarkable improvement in the spin relaxation times at $[\text{NV}] = 0.6$ –1.3 ppm.

Having characterized the optical-spin properties of the ^{12}C , N-NDs, we feed these NDs to cultured HeLa cells to perform CW and pulsed ODMR experiments inside live cells. We fabricated a culture device by bonding a multiwell acrylic frame to coverslips with a notch-shaped antenna and cultured the HeLa cells in the wells (see Fig. S8a). Subsequently, we introduced ^{12}C , N-NDs into the cells via endocytosis (see Methods). Figure 4a shows a merged bright-field and red-fluorescence image of ND-labeled HeLa cells. The two NDs in Fig. 4a (designated as ND1 and ND2) are sufficiently bright to distinguish in the presence of autofluorescence in the cells. Figure 4b indicates that the brightness of ND1 and ND2 on the yellow dotted lines in Fig. 4a is saturated or near saturation, whereas the background fluorescence is nearly zero.

We measured and observed narrow and deep ODMR spectra of ND1 and ND2 inside the cells (Fig. 4c). Fluorescence fluctuations owing to Brownian motion were observed during the CW-ODMR measurements. We performed pulsed ODMR measurements on ND2 under an external magnetic field in a similar manner to that described above. The Brownian motion significantly affected the pulsed ODMR data when the microwave was applied because the random fluctuation of the ND orientation appears as dephasing during the signal integration [40] (see Figs. S8c–e). All-optical T_1 relaxometry is an exception, which utilizes time-dependent spin polarization after optical initialization [18] (Fig. 4d). The profile exhibited a millisecond-scale relaxation. Double exponential fitting gives a value of $T_1 = 0.87$ ms, which is six times larger than the mean T_1 value of type-Ib NDs. In contrast, the T_2 relaxation profiles exhibit a substantial shortening of T_2 owing to the Brownian motion. Figure 4e shows the relaxation profile of the $\pi/2$ -spin-echo sequence. Single-exponential fitting yields $T_2 = 67.5$ ns, which is one order of magnitude shorter than the mean T_2 value determined above. The difficulties associated with the Brownian motion of NDs during pulsed ODMR measurements have been previously discussed [41]; however, to date, this phenomenon has not been actively investigated owing to the very short T_2 in type-Ib NDs. The NV spin coherence of the present ^{12}C , N-NDs will enable to develop advanced pulsed ODMR quantum-sensing pro-

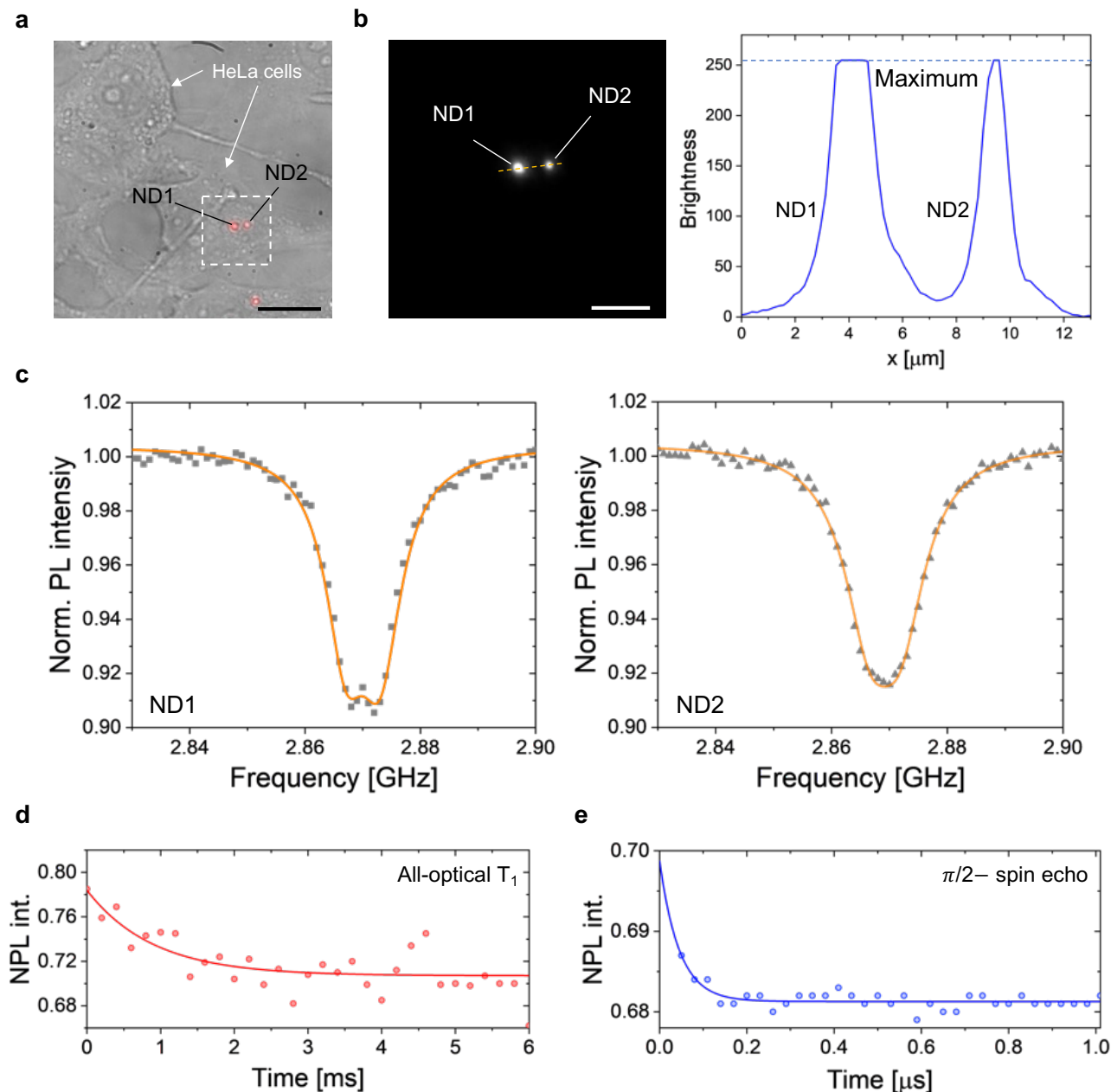


FIG. 4. (a) Merged microscope image of gray bright-field and red fluorescence for HeLa cells uptaking ^{12}C , N-NDs (Scale bar: 25 μm). (b) Red fluorescence (ND1, ND2) in the white dotted box of Fig. 4(a) (Scale bar: 10 μm), and a cross-section along the yellow dotted line exhibiting the brightness of ND1 and ND2 (maximum value: 256). (c) In-situ ODMR spectra of ND1 and ND2 in the live cells. (d) All-optical T_1 relaxometry and (e) $\pi/2$ -spin echo profiles for ND2.

protocols against the Brownian motion.

DISCUSSION

This study demonstrates a remarkable improvement in the NV spin properties of ultrabright NDs with $[\text{NV}] = 0.6\text{--}1.3$ ppm. Microwave irradiation may result in heat generation and damage biological samples. Thus, the observed high contrast of the CW-ODMR spectra and up

to a 16-fold reduction in microwave power are promising features for biological applications. The ^{12}C , N-NDs exhibit long average spin-relaxation times of $T_1 = 0.68$ ms and $T_2 = 1.6$ μs , which are close to the bulk diamond limits and are longer than those of the conventional type-Ib NDs by factors of 6 and 11, respectively. This enhancement of the NV spin coherence is principally attributed to the spin-impurity control. We also confirm that T_2 of the Ib-100 and Ib-600 NDs are close to the bulk-limited

values calculated from their $[NV] = 300\text{--}540$ ppm, which is estimated from their infrared absorption spectra (see Supplementary Information). The spin-impurity control is thus critical to improve the NV spin characteristics of the NDs with a size of $\gtrsim 80$ nm. The present T_1 extension increases the relaxometric signal-to-noise ratio (SNR) in Gd^{3+} detection [15]. Further, the ^{12}C , N-NDs can improve the SNR by a factor of six compared with that of the type-Ib NDs, thus potentially lowering the detection limit for reactive oxygen species [18]. Similarly, the 10-fold T_2 extension increases the measurement sensitivity in AC magnetometry by a factor of three [42], thus allowing the implementation of various T_2 -based quantum measurement protocols, such as advanced spin-echo and thermal-echo quantum sequences in NDs [31, 43].

The proposed ^{12}C , N-NDs pose some technical challenges, including: (i) the inhomogeneity in the NV characteristics should be further minimized, (ii) pulsed-ODMR protocols against Brownian motion must be established, and (iii) large-scale production of NDs is required. First, the inhomogeneity in the NV characteristics may arise from the spatial variations in the NV spins inside the original single crystalline diamonds because of several factors, such as different growth sectors, atomic concentrations, and dislocations [44, 45]. Further, surface spin noises can fluctuate the NV characteristics of each ND because of inhomogeneous surface termination, e.g., different types and contents of dangling bonds, causes variations in the surface spin noise [46, 47]; these inhomogeneity factors may vary T_1 and T_2 (Figs. 3e, f). In the present study, the variations in T_1 and T_2 observed in the case of the ^{12}C , N-NDs are comparable with those for the Ib-100 and Ib-600 NDs. Therefore, these variations need to be further minimized to improve the measurement accuracy of quantum sensors employed in biomedical applications [18].

Inhomogeneity in the NV spin environment also affects the pulsed ODMR, particularly through T_2^* . According to previous studies, T_2^* of the NV ensembles in high-NV-density type-Ib NDs was reported to be extremely short (< 100 ns) based on the assumption that it could not be measured [48]. Further, the measurement of pulsed ODMR, including Rabi oscillations and $3\pi/2$ -spin echo, becomes challenging when the ND size increases (Ib-100 and Ib-600; see Figs. S7a–d, Fig. S10a) because of the increased inhomogeneity in the NV spin environment. In contrast, we observed clear Rabi oscillations and spin-echo inversion of the $3\pi/2$ -spin echo in the ^{12}C , N-NDs (Figs. S6j–i, Fig. S10a), indicating long T_2^* for the NV ensembles. Indeed, we observed Ramsey oscillations for a certain ^{12}C , N-ND with $T_2^* = 140$ ns (Figs. S10b, c), while a statistical analysis was impossible because of the low success probability; this particular ND might have an excellent NV spin environment owing to the present spin-impurity control.

Second, pulsed ODMR measurements must be opti-

mized for NDs exhibiting Brownian motion. In the pulsed ODMR experiments, both the T_1 and T_2 profiles show substantial shortening of the relaxation times, except for the all-optical T_1 relaxometry, that is, when microwave spin manipulations are involved. NDs exhibit Brownian motion inside the cells, and the rotation of the NV orientation relative to the microwave magnetic field fluctuates. During signal integration in the present measurement protocol, this effect modulates the spin signal, effectively shortening the microwave T_1 and spin-echo decays [40]. Only all-optical T_1 relaxometry provides a profile similar to that observed for stationary NDs. Therefore, integrating pulsed ODMR protocols is necessary to adapt to random orientations and motion [49, 50].

Finally, the large-scale production of ^{12}C , N-NDs is required for further biochemical applications. Batch reactions for the surface functionalization of NDs require more than 10 mg of NDs to obtain higher yields [10]. Currently, the number of single crystals with reduced spin impurities and high-density NV is insufficient because of the special production processes involving ^{12}C methane and the absence of a mass production line. Furthermore, the milled NDs are centrifuged to separate the fractions with different sizes of NDs, which substantially reduces the final amount of NDs. The optimization of both the production process and the cost is important for achieving large-scale production.

In conclusion, we demonstrated the development of ultrabright spin-impurity controlled NDs containing $[NV]_{^{12}C,N} = 0.6\text{--}1.3$ ppm with spin impurities of $[^{12}C] = 99.99\%$ and $[N] = 30\text{--}60$ ppm. The NDs exhibit a 50–700 nm size range and are readily used for the fluorescent labeling of cultured cells. We demonstrated a remarkable improvement of the NV spin quality as compared to that of the conventional type-Ib NDs including narrow and deep CW-ODMR spectra and the extended average spin-relaxation times of $T_1 = 0.68$ ms and $T_2 = 1.6$ μ s (1.6 ms and 2.7 μ s in maximum). We observed that these NDs used 16 times less microwave power to reach a 3% ODMR contrast than their type-Ib counterparts. Using these ^{12}C , N-NDs, we performed ODMR measurements (CW-ODMR, T_1 and T_2) inside the cells. These results successfully demonstrate the pertinence of quantum-grade NV spin properties for quantum sensing in potential biological applications.

METHODS

ND preparation

^{12}C -isotope-enriched single-crystalline bulk diamonds with controlled nitrogen concentrations were synthesized using the HPHT method as described previously [51], with minor modifications for single-crystal growth. The ^{12}C enrichment was 99.99% and the nitrogen concentration was 30–60 ppm, as confirmed via secondary ion mass spectroscopy (SIMS) after HPHT growth. NV centers were generated in these bulk diamonds using electron beam irradiation (3 MeV , $1 \times 10^{18}\text{ cm}^{-18}$) under ambient conditions, followed by vacuum annealing at $900\text{ }^\circ\text{C}$ for 1 h [52]. These bulk diamonds were pulverized, followed by suspension in water to obtain ^{12}C , N-NDs. Type-Ib NDs with mean sizes of 100 and 600 nm were purchased from Adámas Nanotech. (NDNV100nmHi, NDNV600nmHi).

ND coating on the coverslips and AFM

To determine the NV concentration of ^{12}C , N-NDs, coverslips with engraved island grids on one side was used. A small droplet of the ND suspension was drop-casted onto a coverslip, enabling the utilization of the same NDs for brightness confirmations and AFM measurements. The topographies of the spin-coated samples were determined using AFM in the tapping mode (SPA400, Hitachi High-Tech Corporation) after the ODMR measurements. The height of the ND topography was regarded as the ND size to avoid the tip convolution effect [53–55]. The images were collected at a scan rate of 0.1–0.5 Hz.

Optical and ODMR measurements

The optical properties and ODMR of the NDs were measured using a lab-built confocal fluorescence microscope with a microwave excitation system based on previous studies [34, 38, 56]. A 532-nm laser was used to excite the NDs with an intensity in the $5\text{--}10\text{ kW cm}^{-2}$ range, which corresponds to an optical saturation parameter of $s = 0.05 - 0.10$ [38, 57]. For the excitation and the fluorescence collection, a 50x dry objective with a numerical aperture of 0.7 mounted on a piezo actuator (Piezosystemjena, MIPOS 100) for fine z-axis adjustment was used. A voice-coil-driven fast-steering mirror (Optics In Motion, OIM101) was used for fast xy-scanning of the laser. NV fluorescence was filtered using a dichroic beam splitter (Semrock, FF560-FDi01) and a long-pass filter (Semrock, BLP01-635R-25) to remove residual green laser scattering. The fluorescence was coupled to an optical fiber (Thorlabs, 1550HP) and

detected using a single-photon counting module (Excelitas, SPCM-AQRH-14), and its spectra were measured using a spectrometer equipped with a charge-coupled device camera (Princeton Instruments, PIX256OE-SF-Q-F-A). The output from the photon-counting module was fed into a board system (National Instruments USB-6343 BNC). The laser scanning was controlled using a lab-built program using GPScan [58] in part. In the ODMR measurements for both the continuous-wave (CW) and pulsed modes, microwaves were generated using a signal generator (Rohde & Schwarz, SMB100A) and sent to radiofrequency (RF) switches (Mini-circuit, ZYSWA-2-50DRS and General Microwave, F9160) triggered by a bit-pattern generator (SpinCore, PBESR-PRO-300). The signal was then amplified using a 45 dB amplifier (Mini-circuit, ZHL-16W-43+). In the CW mode, microwave excitation was gated using the RF switches to suppress noise ($200\text{ }\mu\text{s}$ for microwaves on and off). In the pulsed mode, external magnetic fields of 5–15 G were applied along the NV quantization axis using a small neodymium magnet mounted on a multi-axis manual stage to lift the degeneracy of the magnetic sublevels and detect Rabi-nutations in the pulsed measurements. The pulse operation of the excitation laser was implemented using an acousto-optic modulator (AOM, G&H, 3200-121), and NV spins were optically initialized using a $3\text{ }\mu\text{s}$ pulse width. All pulse sequences are presented in Fig. S3b–d. To determine the duration of π pulse for the NV spins, Rabi measurements were performed, and the profile was fitted with a sine-damping function. T_2 was measured using spin-echo sequences, and $\pi/2 - \pi - \pi/2$ ($\pi/2$ -spin echo) and $\pi/2 - \pi - 3\pi/2$ ($3\pi/2$ -spin echo) sequences were measured to cancel common-mode noise [59]. T_1 was measured using spin-polarization relaxometry sequences. We measured all-optical T_1 and microwave T_1 relaxometry sequences, separately and cancelled the common-mode noise by subtraction [39].

CW-ODMR spectral analysis

The observed ODMR spectra were fitted using a double-Lorentzian function ($y(x)$) composed of two Lorentzian functions, $L_{1,2}(x)$: $y(x) = y_0 + L_1(x) + L_2(x)$, and $L_{1,2}(x) = (2A_{1,2}/\pi)[w_1/(4(x-x_{1,2})^2 + w_{1,2}^2)]$, where, y_0 , $A_{1,2}$, $w_{1,2}$, and $x_{1,2}$ are the offset, peak area, linewidth, and peak position frequency of $L_{1,2}(x)$, respectively. The following boundary conditions were applied to the fitting: $2.862 \leq x_1 \leq 2.870$ and $2.870 \leq x_2 \leq 2.878$. The “Norm. PL intensity” in Fig. 2d were determined by taking the mean of the two peaks $[y(x_1) + y(x_2)]/2$. In this study, the spectral parameters for the peak splitting E and zero-field splitting D were determined using the fitting parameters $E = x_2 - x_1$ and $D = (x_1 + x_2)/2$, respectively (Figs. 2e, f). E is the strain-induced parameter [60–62]. Further details of the

fitting procedure are provided in the Supplementary Information (Fig. S5a).

Analysis method for the T_1 and T_2

The raw T_1 relaxation profiles showed large amount of noise, which destabilized the subsequent fitting processes. These noises were numerically filtered by taking a moving average over nine data points (out of a total of 50 points), and the filtered profiles measured with the all-optical T_1 and microwave T_1 sequences were subtracted (see Fig. S6a–f). The subtracted T_1 profiles were fitted using a two-phase exponential decay, $C = C_0 + A_1 \exp(-(\tau - t_0)/t_1) + A_2 \exp(-(\tau - t_0)/t_2)$, where C_0 is the common offset and $A_{1,2}$ and $t_{1,2}$ are amplitudes, and time constants, respectively. Out of the two decay times, the longer one was used as T_1 ($T_1 = \max(t_1, t_2)$) as previously described [63–67]. Similarly, the $\pi/2$ - and $3\pi/2$ -spin-echo profiles were filtered by moving the average over five data points (out of a total of 50 points) before their subtraction. For the ^{12}C , N-NDs, the subtracted profiles were fitted using the stretched exponential decay $\exp(-(\tau/T_2)^{1.5})$ to determine T_2 [28] (see Figs. S6a–c). For the T_2 determination of the type-Ib NDs, this fitting is only applied to the $\pi/2$ -spin echo profiles because $3\pi/2$ -spin echo sequence did not provide spin-echo amplitudes owing to the short T_2^* (see Supplementary Information).

ND labeling of HeLa cells

HeLa cells were cultured in a cell culture medium (DMEM containing 4500 mg/mL glucose, 10% FBS, 100 U mL⁻¹ penicillin/streptomycin, and phenol red) in a well that was fabricated on a coverslip, with a notch-shaped antenna on the other side (see Fig. S8a). The glass surface of the device (well side) was coated with collagen to improve cell adhesion. ND labeling of cells was performed using the method described previously [68, 69]. A suspension of ^{12}C , N-NDs was added to the culture medium, and the cells were incubated at 37 °C and 5% CO₂ for 24 h. The cells were then washed gently three times with phosphate-buffered saline and immersed in a culture medium without phenol red to perform the ODMR measurements.

FTIR measurements

The nitrogen concentration in the type-Ib NDs was estimated by measuring 150- μm -sized type-Ib diamond micro-crystals (Adámas Nanotech., MDNV150umHi) from the same product line using the Fourier transform infrared (FTIR) spectroscopy, as previously re-

ported [70, 71]. A Jasco FTIR6200-IRT7000 micro Fourier-transform spectrometer was used with a KBr/Ge beam splitter, a ceramic light source, and MCT detector. The micro-crystals were placed on a copper mesh with pore sizes of 85 μm , and near-infrared (NIR) light was focused with a spot size of 50–100 μm through Cassegrain optics in the transmission mode. The sample chamber was purged with nitrogen gas to minimize atmospheric background in the spectra. The spectral data were accumulated 512 times with a spectral resolution of 4 cm⁻¹. From the obtained spectrum, the nitrogen concentration [N] (ppm) was determined using the following relationship: $(\mu_{1130\text{cm}^{-1}}/\mu_{2120\text{cm}^{-1}}) \times 5.5 \times 25$, where μ is absorption intensity for the given wavenumber [72].

ACKNOWLEDGMENTS

The authors thank I. C. Barbosa, O. Benson, H. Ishiwata, Y. Masuyama, R. Schirhagl, S. Sakakihara, T. Schröder, T. Teraji, S. Yamashita for fruitful discussions and technical assistance with the experiments. A part of this work was supported by ARIM of MEXT (JPMXP1223OS1022) and IPM, Okayama University under joint-use facilities framework. This study was partially supported by JSPS-KAKENHI (M.F. and Y.S. 20H00335. M.F.: 20KK0317. Y.S.: 21H05599.) and JST-ASPIRE (Y.S. and M.F.: JPMJAP2339). K.O. acknowledges funding from JST (JPMJFS2128) and JSPS (23KJ1607). S.M. acknowledges funding from JST (JPMJSP2126). M.F. acknowledges funding from NEDO (JPNP20004), AMED (JP23zf0127004), JST (JPMJMI21G1), RSK Sanyo Foundation, and Asahi Glass Foundation. Y.S. acknowledges the funding from JST-PRESTO (JPMJPR20M4).

AUTHOR CONTRIBUTIONS

K.O., M.T., Y.N., and M.F. conceptualized the research. M.T., H.T., and Y.N. prepared ^{12}C , N-NDs. K.O., H.N., S.M., H.K., and M.F. performed NV spin characterization and cellular experiments. K.O. and T.A. performed the ND size determination using AFM. K.O., Y.S., and M.F. analyzed the NV spin data. All the authors participated in the discussion and writing of the manuscript.

SUPPLEMENTARY INFORMATION

Determination of the NV concentration in NDs with size–brightness correlation

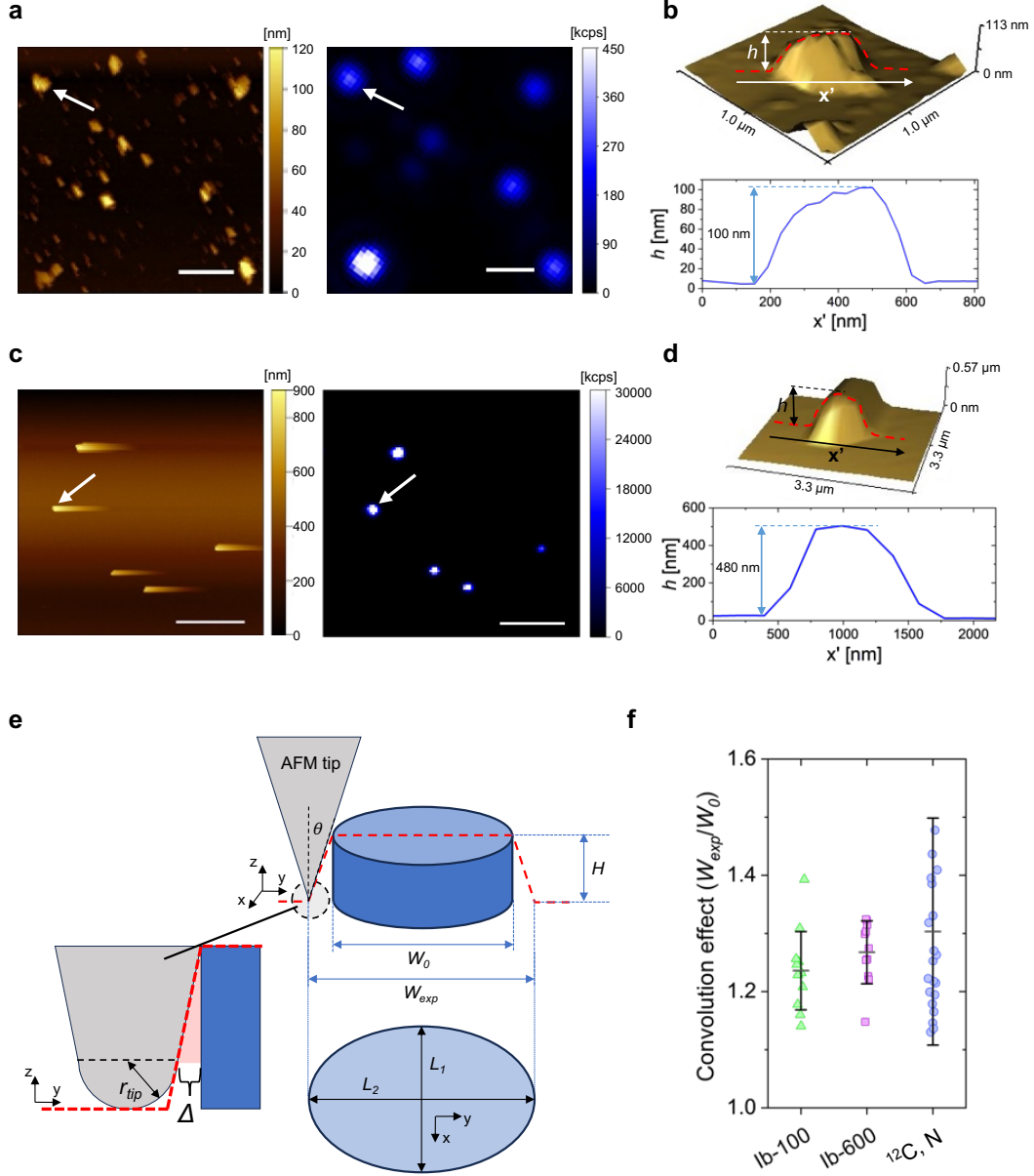


FIG. S1. (a) AFM topography (left) and the corresponding confocal fluorescence (right) images of Ib-100. Scale bar; 1 μm . (b) Three-dimensional visualization of the topography of the ND indicated by the white arrow in Fig. S1a (top) with a cross-section along x' axis (bottom). (c) AFM topography (left) and the corresponding confocal fluorescence (right) images of Ib-600. Scale bar; 10 μm . (d) Three-dimensional visualization of the topography of the ND indicated by the white arrow in Fig. S1c (top) with a cross-section along x' axis (bottom). (e) Schematic of the AFM measurements with the convolution effect. W_{exp} , W_0 , H , r_{tip} , and θ are the experimental, true length in the xy -imaging plane of the measured sample, height of the sample from the xy -imaging plane, AFM tip radius, and tip angle, respectively. L_1 and L_2 are the ND width in the x and y axes, respectively. $r_{tip} = 10$ nm, $\theta = 20^\circ$. Red dotted line: the convolution effect of the AFM tip. (f) Statistical plots of the convolution effect (W_{exp}/W_0) for Ib-100, Ib-600 and ^{12}C , N-NDs. Mean and standard deviation (1σ) are indicated in the statistical plots.

Figures S1a–d show AFM topology and confocal images of the type-Ib NDs (Ib-100, Ib-600). These AFM topography images, including Figs. 1d, e for ^{12}C , N-NDs, have a common artifact: convolution caused by interaction between

sample and AFM tip. Figure S1e shows a schematic of this convolution effect in the AFM measurements of NDs. The experimentally determined width of the NDs (W_{exp}) in the xy-imaging plane can be written as [53]:

$$\begin{aligned}\frac{1}{2}W_{exp} &= r_{tip} + \Delta + \frac{1}{2}W_0 \\ \Delta &= (H - r_{tip}) \tan \theta\end{aligned}\quad (S1)$$

where W_0 , H , r_{tip} , and θ are ND width in the xy-imaging plane, ND's height from the xy plane (glass surface), tip radius, and tip angle, respectively. In the real NDs, the widths in the x and y axes ($L_{1,2}$) differ because of the asymmetric shape and we adopted their mean values as W_{exp} for simplicity. The term of $r_{tip} + \Delta$ indicates the tip convolution. From this analysis, we calculated W_{exp}/W_0 to show how much convolution effect exists in the present three types of NDs (Ib-100, Ib-600, ^{12}C , N-NDs). As shown in Fig. S1f, the results indicate that the convolution effect is comparable to each other among these samples.

After determining W_0 , we calculated $[\text{NV}]$ as follows. We first assumed that the fluorescence intensity is proportional to the number of NVs as the optical excitation intensity is far below the saturation ($s \approx 0.05$). As the number of NVs is proportional to the ND volume, the fluorescence intensity can be written as

$$I \propto [\text{NV}]V, \quad (S2)$$

where I and V are the fluorescence photon-count rate and the volume of NDs, respectively. By taking a ratio of the fluorescence intensity for the two types of the NDs, $[\text{NV}]$ can be determined as follows:

$$[\text{NV}]_j = [\text{NV}]_i \frac{I_j V_i}{I_i V_j}, \quad (S3)$$

where the subscripts i, j indicate the type of the NDs. By introducing aspect ratio ($A = W_0/H$), V can be expressed as

$$V = kH^3g(A) \quad (S4)$$

where k and $g(A)$ denote morphology dependent factor and A -dependent conversion factor, respectively (e.g, $k = \pi/6$, $g(A) = 1$ for sphere, $k = 1$, $g(A) = 1$ for cube, $k = \pi/4$, $g(A) = 1$ for cylinder, as shown in Fig. S2a).

We then estimated the NV concentration of the ^{12}C , N-NDs. In Fig. 1g, the fluorescence photon-count rate of Ib-600 NDs was approximately 150 times more than that of Ib-100 ($I_{\text{Ib600}}/I_{\text{Ib100}} \approx 150$). Provided both of the ND morphology as $A = 1$ type such as cubic, Ib-600 NDs were found to be approximately 130 times larger in volume than Ib-100 NDs ($V_{\text{Ib600}}/V_{\text{Ib100}} \approx 130$). Through Eq. S3 and Eq. S4, these parameters give $[\text{NV}]_{\text{Ib600}} \approx 1.2[\text{NV}]_{\text{Ib100}}$, comparable to the ratio determined from their specification sheet ($[\text{NV}]_{\text{Ib100}} = 3$ ppm, $[\text{NV}]_{\text{Ib600}} = 3.5$ ppm). Similarly, assuming the premise of ^{12}C , N-NDs having $A = 1$ type morphology, we estimated $[\text{NV}]_{^{12}\text{C},\text{N}}$ to be $0.26[\text{NV}]_{\text{Ib100}} \approx 0.6$ ppm or $0.20[\text{NV}]_{\text{Ib600}} \approx 0.8$ ppm by taking a reference to Ib-100 or Ib-600 NDs, respectively.

We also estimated $[\text{NV}]_{^{12}\text{C},\text{N}}$ for a $A \neq 1$ morphology such as disk-like ND structures ($k = 1$, $g(A) = A^2$ in Eq. S4). Figure S1b shows statistical plots of A by analyzing the AFM data of the NDs. From this data, we obtained A^{mean} for Ib-100, Ib-600 and ^{12}C , N-NDs to be 3.9 ± 1.2 , 2.9 ± 0.8 and 3.3 ± 1.6 , respectively. These values are comparable to the previous study about 140 nm NDs, where the NDs have the disk-like shape with $A \approx 3$ [37]. Note that we analysed only one length of NDs (either of L_1 and L_2) using the tailed AFM topography image caused by the measurement limitation of AFM tapping mode (Fig. S1c), so that it is possible that the calculated aspect ratio of Ib-600 can become slightly smaller value than that of Ib-100. Figures S2c–e show volume-brightness correlation plots of the type-Ib NDs and ^{12}C , N-NDs for $A = 1$ and $A \neq 1$ (disk-like cylinder) cases. The scatter plots were entirely shifted to the larger side for all of the ND types, when the volume estimation method was switched from $A = 1$ to $A \neq 1$. Using this disk-like-cylinder shape with $A \neq 1$, we obtained $0.44[\text{NV}]_{\text{Ib100}} \approx 1.3$ ppm or $0.21[\text{NV}]_{\text{Ib600}} \approx 0.6$ ppm by taking a reference to Ib-100 or Ib-600 NDs, respectively. Therefore, we determined $[\text{NV}]$ of the present ^{12}C , N-NDs was 0.6–1.3 ppm.

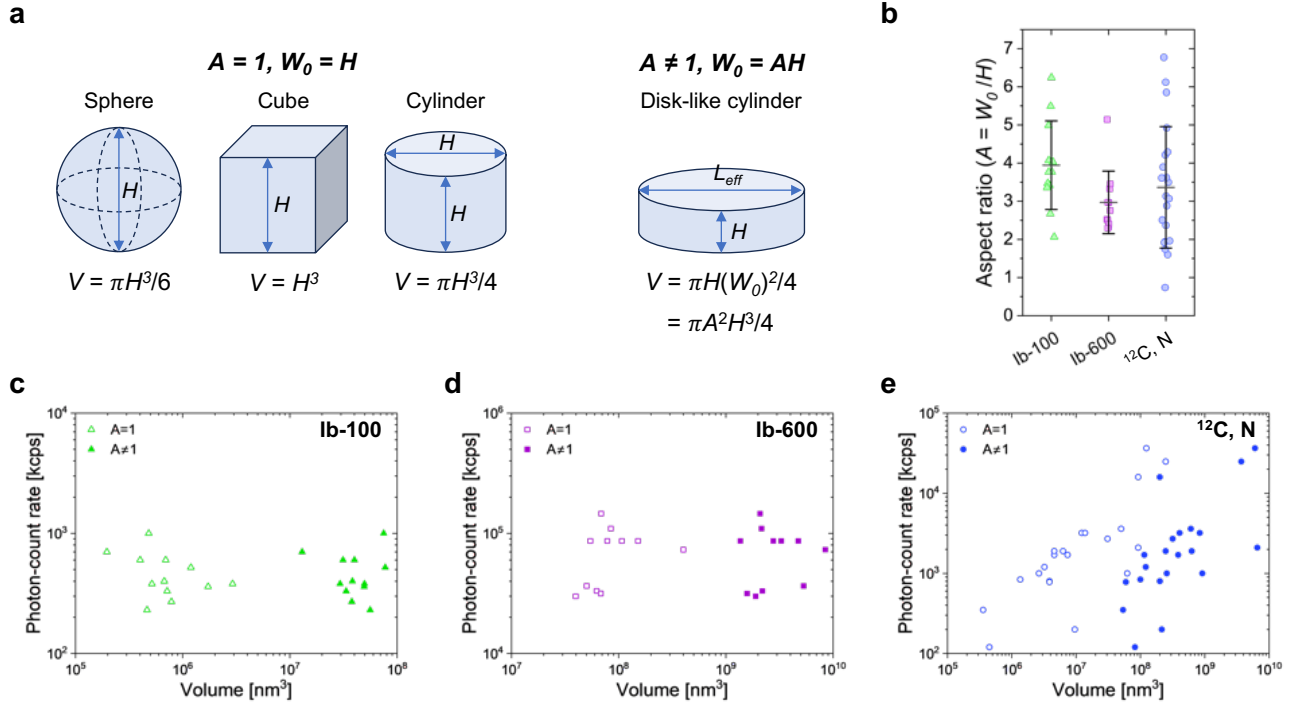


FIG. S2. (a) Schematic images of the typical ND morphology with their parameters defining the shapes. A , V , H , and W_0 indicate aspect ratio, volume, width, and height, respectively. (b) Statistical plots of the aspect ratio for Ib-100, Ib-600 and ^{12}C , N-NDs. Mean and standard deviation (1σ) are indicated in the statistical plots. Plots of the ND photon counts against the ND volume in the case of the cylinder with $A = 1$ and $A \neq 1$ for (c) Ib-100, (d) Ib-600, (e) ^{12}C , N-NDs.

ODMR Experimental Setup

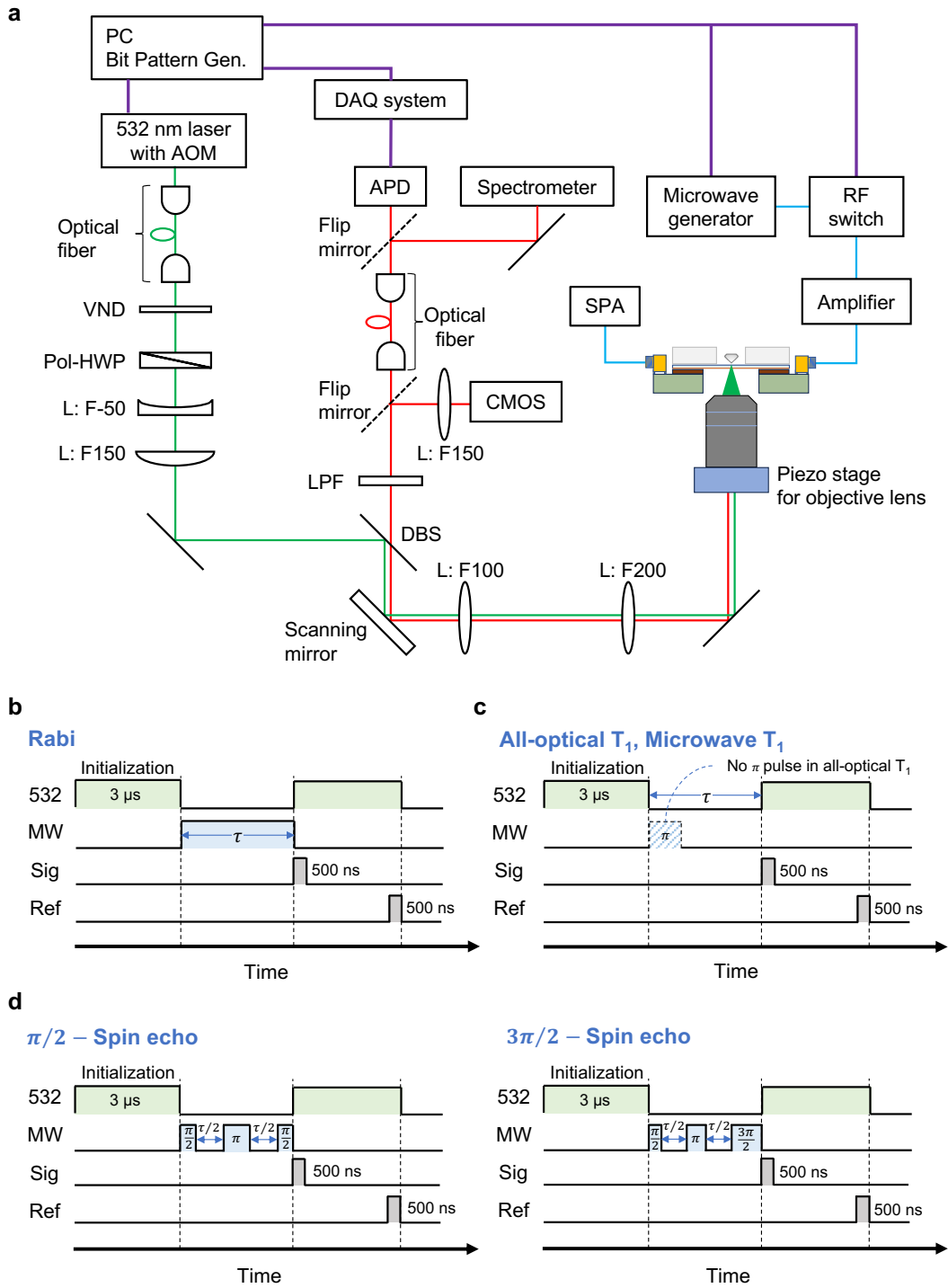


FIG. S3. (a) Schematic of the ODMR setup comprising confocal fluorescence microscope and microwave excitation system. AOM: acousto-optic modulator. VND: variable neutral density filter. Pol-HWP: polarizer and half-wave plate. L: lens. DBS: dichroic beam splitter. LPF: long pass filter. CMOS: complementary metal oxide semiconductor. APD: avalanche photodiode. SPA: spectrum analyzer. RF: radio frequency. Schematic pulse sequences for (b) Rabi, (c) all-optical T_1 , microwave T_1 , and (d) $\pi/2$, $3\pi/2$ -spin echo measurements.

Loss/gain analysis of microwave excitation system including antenna characterization

Figures S4a, b show the geometrical structure of a notch-shaped antenna on a coverslip and the experimentally measured S-parameters, respectively. Table S1 summarizes the losses and gains of the individual components of the microwave system in the ODMR setup. The microwave losses in SMA cables and RF switches were obtained from their specification sheets, and we assumed a minimum gain of +40 dB for the amplifier, considering the high-impedance matching between the cables and the antenna. The loss of the antenna on the PCB at the input (L_R) and output ports (L_T) was calculated from the observed S_{11} and S_{21} values using the following equation [38]:

$$L_R = 10 \log_{10} \left(1 - 10^{\frac{S_{11}}{10}} \right), \quad (\text{S5})$$

$$L_T = \frac{S_{21}}{2}. \quad (\text{S6})$$

The applied microwave power was calculated from the corresponding S-parameter values (Fig. S4b–d), and they were converted from dBm to mW.

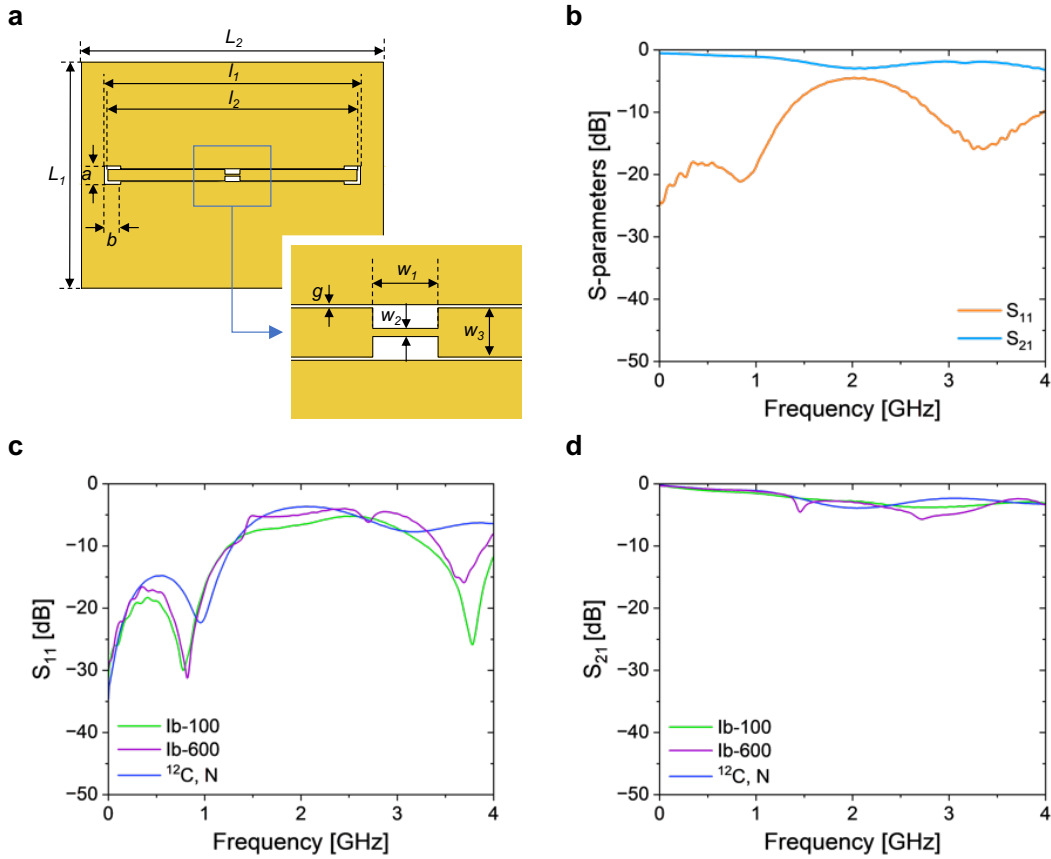


FIG. S4. (a) Geometrical structure of the notch-shaped antenna patterned on the coverslip with dimensions as follows: $L_1 = 30$ mm, $L_2 = 40$ mm, $l_1 = 33.94$ mm, $l_2 = 33$ mm, $a = 2.44$ mm, $b = 2.17$ mm, $g = 0.10$ mm, $w_1 = 2.0$ mm, $w_2 = 250$ μm , and $w_3 = 1.5$ mm. (b) Experimentally measured S_{11} and S_{21} spectrum in the experiment of Fig. 2c (c) Experimentally measured S_{11} and (d) S_{21} spectrum of the antenna used for the experiments of type-Ib NDs and ^{12}C , N-NDs presented in Figs. 2d–f.

TABLE S1. List for microwave input power, loss and gain of the microwave components

Components	Loss or Gain [dB]	Power [dBm]	Notes
Microwave generator		-16.0	The experiment of the Fig. 2c (bottom)
RF switches	-3.5	-19.5	Total insertion loss
Microwave amplifier	+40.0	20.5	Amplifier gain
Microwave cables	-5.0	15.5	Total insertion loss
Antenna reflection loss	-0.386	15.1	$S_{11} = -11.0$
Antenna insertion loss	-0.955	14.2	$S_{21} = -6.32$
Total in the detection area		14.2 [dBm]	

The magnetic field of the microwaves ($|\mathbf{B}|$) on the antenna in Fig. 2b was simulated using the finite-element method (COMSOL). Table S2 summarizes the structures and corresponding materials with the relative permittivity ϵ , relative permeability μ , and electrical conductivity σ used for the calculations. The thin gold-patterned layer (~ 300 nm) was regarded as an infinitely thin perfect electric conductor (PEC) in the simulations. A 70-mm-radius sphere surrounding the coverslip was assumed to be a perfectly matched layer with an absorption constant of 10^{-6} at the sphere boundary.

TABLE S2. List of simulation conditions

Structures	Materials
Coverslip (thickness = 0.17 mm)	Borosilicate glass ($\epsilon = 4.6, \mu = 1.0, \sigma = 0.0$ S/m)
Thin gold layer (antenna)	Perfect electric conductor (PEC)
70-mm-radius sphere	Air ($\epsilon = 1.0, \mu = 1.0, \sigma = 0.0$ S/m)

ODMR spectral analysis using a double-Lorentzian function

The ODMR spectra were fitted to a double Lorentzian function comprising two Lorentzian functions (red and blue curves in Fig. S5a):

$$y(x) = y_0 + L_1(x) + L_2(x),$$

$$L_{1,2}(x) = \frac{2A_{1,2}}{\pi} \frac{w_{1,2}}{4(x - x_{1,2})^2 + w_{1,2}^2}, \quad (\text{S7})$$

where y_0 is a common offset, and $A_{1,2}$, $w_{1,2}$, and $x_{1,2}$ are the peak area, line width, and peak position frequency for the left (index: 1) and right peaks (index: 2), respectively. The ODMR depth in Fig. 2e was obtained using $[y(x_1) + y(x_2)]/2$, and the depth in Fig. 2e was depicted as the ‘‘Norm. PL intensity’’. E and D shown in Figs. 2e, f, were calculated using $E = (x_2 - x_1)$ and $D = (x_1 + x_2)/2$, respectively. Note that the effect of the geomagnetic field (~ 0.5 G) [73] on E was insignificant because its potential variation of E is about 1.4 MHz which is comparable to the variations derived from the random NV quantization axes on the coverslip.

Figure S5b shows the amplitudes of $L_1(x_1)$ and $L_2(x_2)$ in the double Lorentzian fitting for all of the measured type-Ib and ^{12}C , N-NDs. The double Lorentzian model gives successful fitting results with comparable peak amplitudes for L_1 and L_2 under the applied boundary conditions (Fig. S5c). However, compared with those of type-Ib, ^{12}C , N-NDs sometimes exhibit asymmetric results with large differences between $L_1(x_1)$ and $L_2(x_2)$ ($\Delta L = |L_1(x_1) - L_2(x_2)|$), which might affect the results of E and D in Figs. 2f,g. The magnitude of ΔL does not affect the ODMR depth, as shown in Fig. 2e, because the contrast was obtained using $(y(x_1) + y(x_2))/2$, which only depends on the sum of $L_{1,2}(x)$.

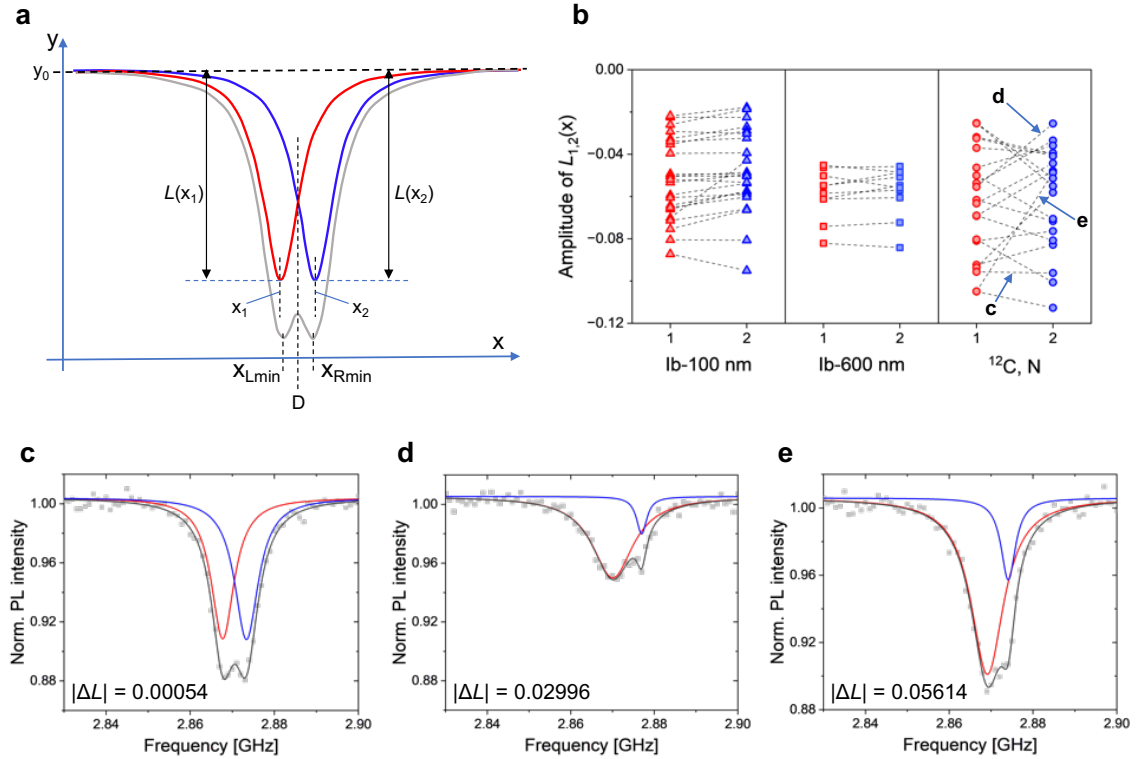


FIG. S5. (a) Schematic of the double-Lorentzian function fitted to the ODMR spectra. (b) Amplitudes of the fitted Lorentzian function ($L_1(x_1)$, $L_2(x_2)$) for the Ib-100, Ib-600, and ^{12}C , N-NDs. c, d, e indicate cases for Figs. S5c, d, e, respectively. (c–e) ODMR spectra with the fitting for the cases specified in Fig. S5b.

To evaluate this effect, we investigated individual fitting cases between NDs with small and large ΔL . We analyzed NDs with small and large ΔL values as representatives of the symmetric and asymmetric cases, respectively (Figs. S5c–e). To estimate the deviation of resulting from fitting destabilization (asymmetry), we compared E (D) values determined using the above defined fitting-based calculations (E_{fit} or D_{fit}) with those by manually taking the frequency

positions of the two peaks of the total double Lorentzian curves: $\Delta E_{\text{man}} = x_{\text{Rmin}} - x_{\text{Lmin}}$ or $\Delta D_{\text{man}} = x_{\text{Lmin}} + x_{\text{Rmin}}$, where $x_{\text{L(R)min}}$ indicates the minimum points of overall double Lorentzian shape (Gray curve in Fig. S5a). Table. S3 summarizes these analyses for the three cases shown in Figs. S5c–e. $E_{\text{fit}} - E_{\text{man}}$ shows primarily positive values (0.74 and 0.71 MHz), and in the case of a large ΔL , it gives a more positive value (2.18 MHz), which means that the fitting destabilization tends to overestimate the E values compared to the apparent peak splitting of ODMR spectra. This result indicates that the observed small E values for the ^{12}C , N-NDs could not be attributed to underestimation from the fitting destabilization; rather, the E values are overestimated. Therefore, we conclude that the present fitting destabilization does not affect the observed tendency of small E values in the ^{12}C , N-NDs.

$D_{\text{fit}} - D_{\text{man}}$ can show both negative and positive values, and the magnitude can increase up to 0.00111 GHz, which is comparable to the observed difference between ^{12}C , N- and type-Ib NDs. Therefore, fitting destabilization may result in the observed tendency of relatively large D values in the ^{12}C , N-NDs. However, the ODMR spectra of ensemble NV exhibit a skirt on the low-frequency side [74]. This low-frequency skirt is more prominent in type-Ib NDs than that in ^{12}C , N-NDs, and it pulls the fitting estimation of D toward the lower-frequency side for type-Ib NDs. Thus, the relatively large D values in the ^{12}C , N-NDs could be attributed to both fitting destabilization and intrinsic asymmetry of ODMR spectral shape in the type-Ib NDs.

TABLE S3. Fitting destabilization for E_{fit} and D_{fit}

Case	ΔL	$E_{\text{fit}} - E_{\text{man}}$ [MHz]	$D_{\text{fit}} - D_{\text{man}}$ [GHz]
Fig. S5c	0.00054	0.74	0.00010
Fig. S5d	0.02996	0.71	-0.00049
Fig. S5e	0.05614	2.18	0.00111

Fitting procedure of the relaxation curves

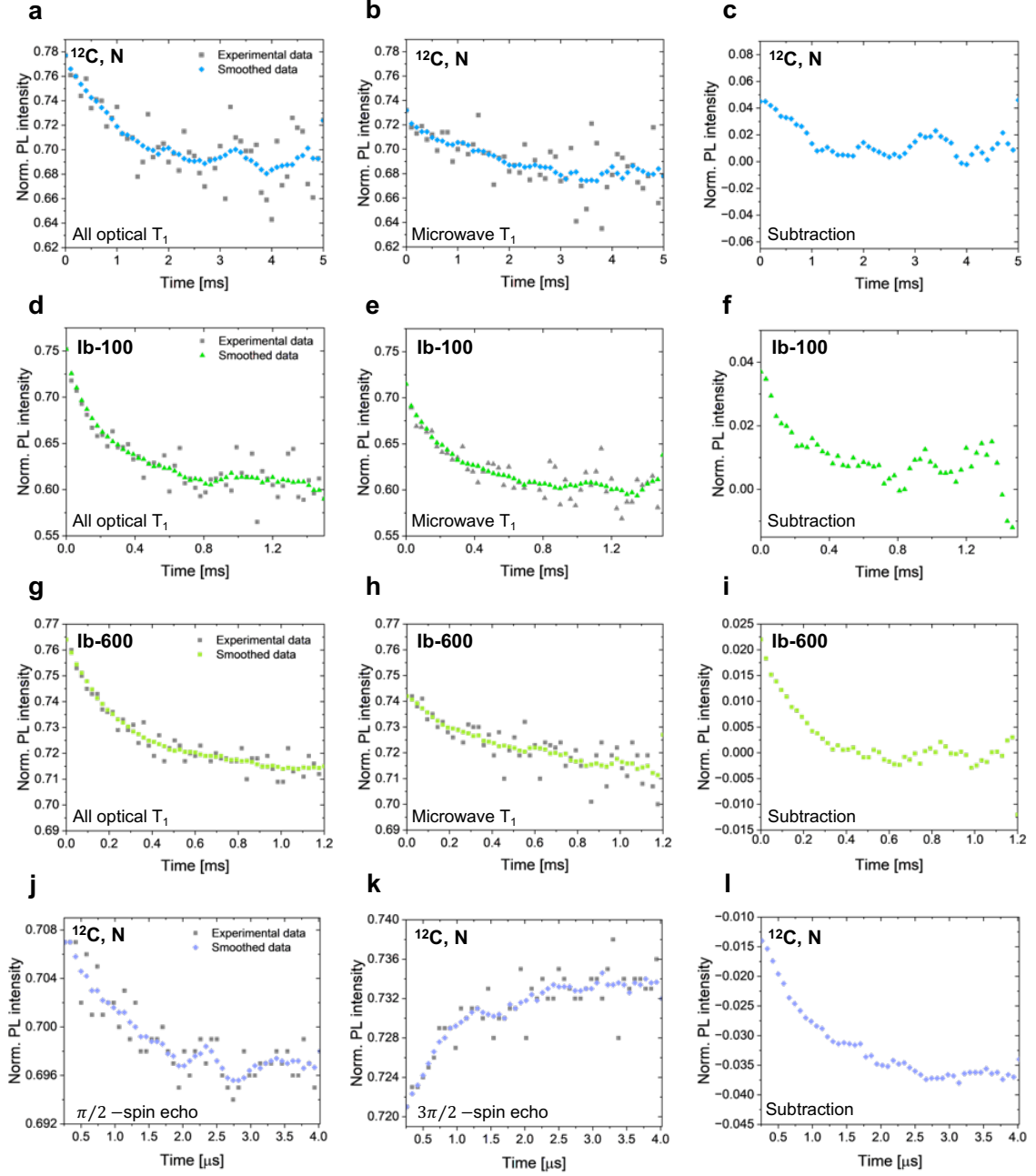


FIG. S6. (a) Representative profiles of all-optical T_1 and (b) microwave T_1 relaxometry for the ^{12}C , N-NDs. (c) The subtracted relaxation profiles. (Grey dots: experimental data, light blue dots: smoothed profiles by the moving average method). (d)–(f) Representative profiles of all-optical T_1 and microwave T_1 relaxometry, and subtracted relaxation for the Ib-100nm NDs. (Grey dots: experimental data, green dots: smoothed profiles by the moving average method). (g) Representative profiles for $\pi/2$ -spin echo, and (h) $3\pi/2$ -spin echo for the ^{12}C , N-NDs. (i) The subtracted profiles. (Grey dots: experimental data, lilac dot: smoothed profiles by the moving average method).

The raw T_1 relaxation profiles showed large noise, which destabilized the subsequent fitting processes. This noise must be numerically filtered to determine T_1 values. The profiles of microwave T_1 and all-optical T_1 were filtered by taking a moving average over nine data points from a total of 50 points and they were subtracted from each other, as shown in Figs. S6a–f (subtracting the microwave T_1 from the all-optical T_1 profile). The subtracted profiles were fitted using bi-exponential decay ($y = y_0 + A_1 \exp[-(\tau - t_0)/t_1] + A_2 \exp[-(\tau - t_0)/t_2]$), as defined in the Methods.

Similarly, the two spin-echo profiles were numerically filtered to remove noise by taking a moving average over five data points with a total of 50 points. The filtered profiles were subtracted to obtain the final T_2 profiles and a stretched exponential decay function $\exp((-\tau/T_2)^p)$ was fitted to determine T_2 . The value of p can vary between 1.47 and 1.50 in the fitting, but we assumed $p = 1.5$ to determine T_2 for all T_2 profiles for the fitting consistency. Note that, in the above analysis of T_1 and T_2 , the particle-based statistical error was adopted for the uncertainty of the mean relaxation times instead of the fitting error because fitting was applied to the numerically filtered data and the time step used in the measurements for the type-Ib and ^{12}C , N-NDs were different.

To determine T_2 of the Ib-100 NDs, we fitted the stretched exponential decay function to the $\pi/2$ -spin echo profiles (Fig. S7a) because the $3\pi/2$ -spin echo profiles did not differ from the $\pi/2$ -spin echo (Fig. S7b), presumably because of the short T_2^* as compared with the microwave π pulse (300–400 ns). For the Ib-600 NDs, the different profiles between $\pi/2$ -spin echo and $3\pi/2$ -spin echo were obtained (Figs. S7c, d), but it was difficult to fit the subtracted profiles in a similar to the case of ^{12}C , N-NDs. Therefore, to determine T_2 of the Ib-600 NDs, we fitted the stretched exponential decay function to the $\pi/2$ -spin echo profiles.

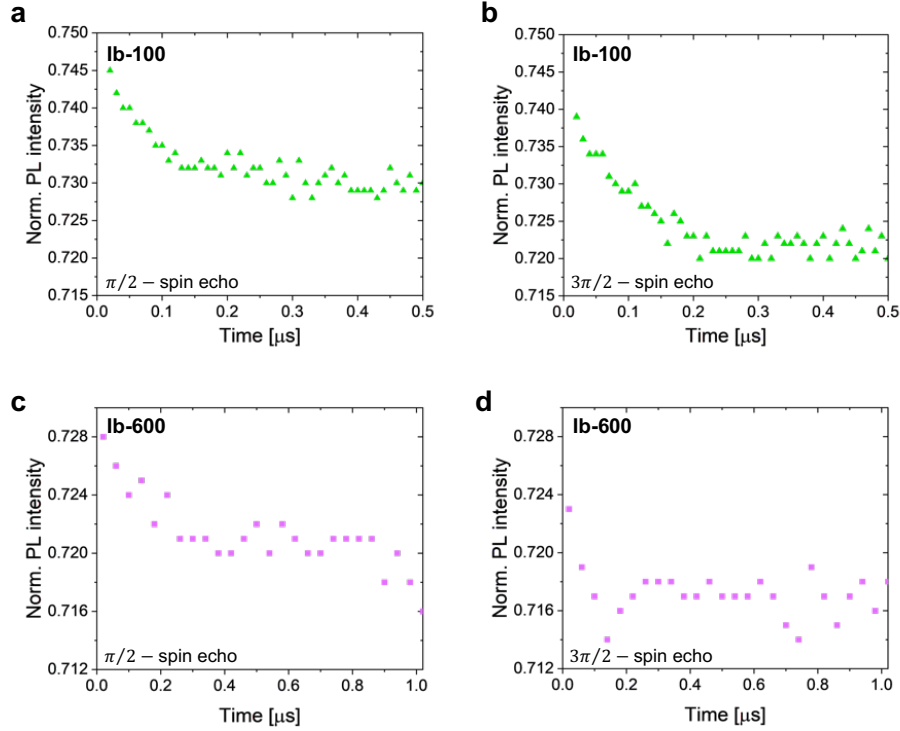


FIG. S7. (a) Representative profiles for $\pi/2$ -spin echo and (b) $3\pi/2$ -spin echo for the Ib-100 (green dots: experimental data). (c) Representative profiles for $\pi/2$ -spin echo and (d) $3\pi/2$ -spin echo for the Ib-600 (purple dots: experimental data).

Cell culture protocol and other experimental results

Figure S8a shows a flow diagram of the cell culture protocol in our home-built multiwell device with a notch-shaped microwave antenna. Figure S8b shows the experimentally measured S_{11} and S_{21} spectra of the multiwell devices containing the cells, respectively. We observed that the ODMR spectral shape changed for 4 min under an external magnetic field in the CW-ODMR measurements for ND1 in the cells (Fig. 4a), indicating the rotation of the NV orientation via rotational Brownian motion. This ND rotation is detrimental when measuring pulsed ODMR profiles under microwave excitation. NDs with 100–300 nm diameters exhibit 0.1–1 kHz (1–10 ms) as the characteristic frequency (time) of the rotational Brownian motion [75]. For example, in the $\pi/2$ -spin echo measurements, a single operation of the sequence with a single echo time finished at approximately 2.0 μs at the longest, however, this spin operation accumulated over 500 ms. After 500 ms of integration, the measurements proceeded to the next sequence with the next echo time. By sweeping the echo time from 20–1020 ns at 40 ns intervals, we obtained a single dataset for the $\pi/2$ -spin echo. Subsequently, the dataset was collected 15 times. The overall measurement time was 3–5 min. The time-varying NV orientation lead to apparent dephasing in the final T_2 profiles. Therefore, interpreting the profiles of microwave T_1 and two spin-echo sequences in the presence of rotational Brownian motion was difficult.

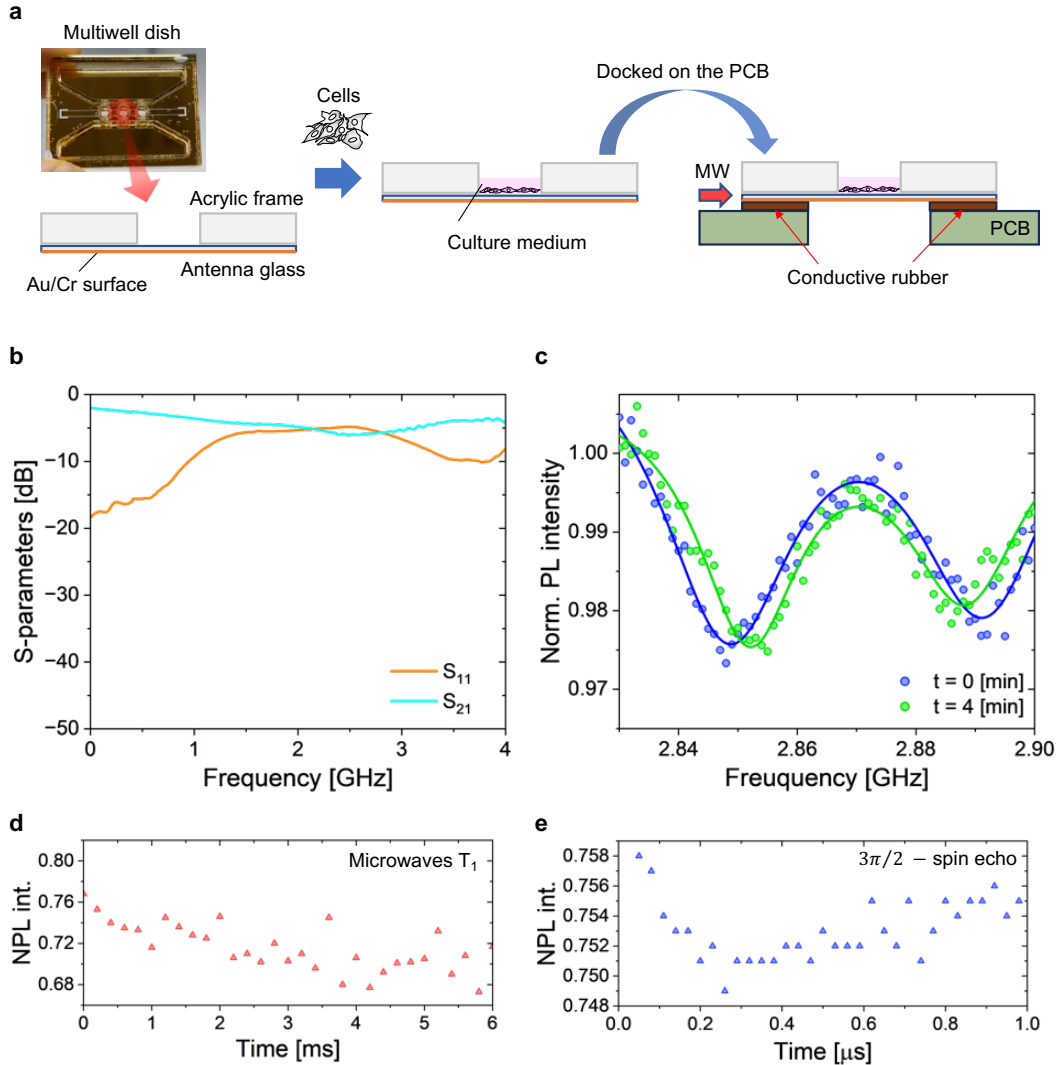


FIG. S8. (a) Flow diagram for the device assembly and ODMR measurements using cells and (b) experimentally measured S_{11} and S_{21} spectra of the device. (c) Split ODMR spectra inside cells under an external magnetic field (blue dots) and the subsequent ODMR spectra of the same NDs in 4 min (green dots). (d) Microwave T_1 and (e) $3\pi/2$ -spin echo for ND2 inside the cell in Fig. 4a.

Determination of nitrogen concentration for type-Ib NDs from FTIR spectrum

SIMS is widely used to determine the nitrogen impurity concentration in bulk diamonds [51]. However, in our case, the crystal size of the type-Ib NDs was too small to be measured using SIMS. EPR spectroscopy can quantify the nitrogen concentration in NDs [76]. However, it requires gram level amount of NDs, which is prohibitively high for the present case. Therefore, we employed FTIR spectroscopy to analyze the concentration of nitrogen in the conventional type-Ib NDs. This measurement was carried out using a Jasco FTIR6200-IRT7000 micro Fourier-transform spectrometer with a KBr/Ge beam splitter and ceramic light source (see Methods). Figure S9a shows a diamond micro-crystal taken from the same product line of the type-Ib NDs used in this study. Figure S9b shows a typical FTIR spectrum of these diamond micro-crystals. From this spectrum, we calculated $(\mu_{1130\text{cm}^{-1}}/\mu_{2120\text{cm}^{-1}}) \times 5.5 \times 25$ to determine the nitrogen concentration [N] (ppm) [72]. The [N] of these micro-crystals was estimated to 300–540 ppm, which was obtained by measuring five crystals in total. The variation in [N] may be caused by several factors, including particulate inhomogeneity, imperfect perpendicular incidence of the NIR beams on the diamond surface because of the unavoidable angle created on the copper mesh during the FTIR measurements.

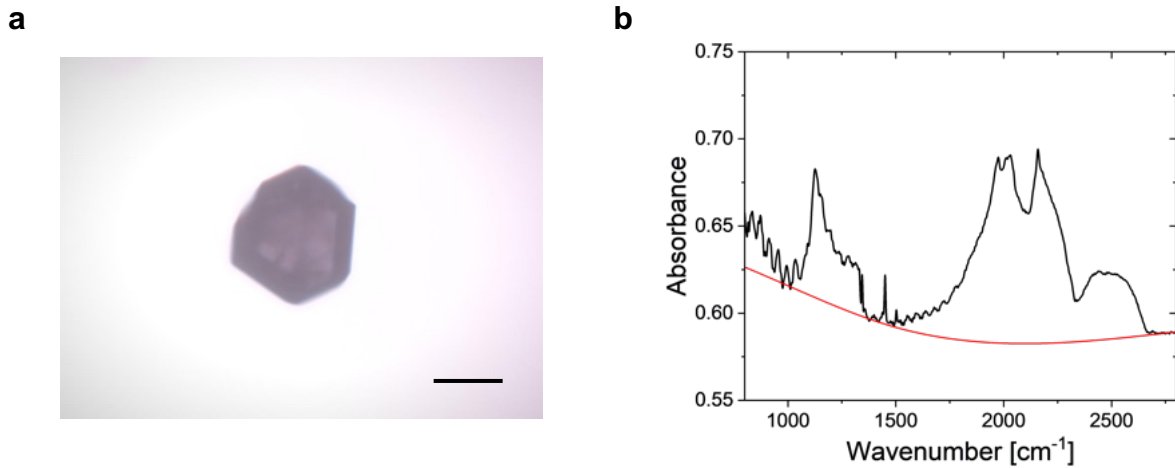


FIG. S9. (a) Microscope image of type-Ib micro-sized diamond in the FTIR measurements. Scale bar: 100 μm . (b) Representative FTIR spectrum for type-Ib diamonds. Red curve: base line.

Rabi oscillation comparison and Ramsey experiments

The inhomogeneity in the NV spin environment diminishes Rabi contrast (Fig. S10a), which makes the subsequent pulsed ODMR measurements challenging particularly for the type-Ib NDs. This inhomogeneity can be evaluated via T_2^* measured by Ramsey experiments (Fig. S10b). Ramsey oscillations for a certain ^{12}C , N-ND is shown in Fig. S10c.

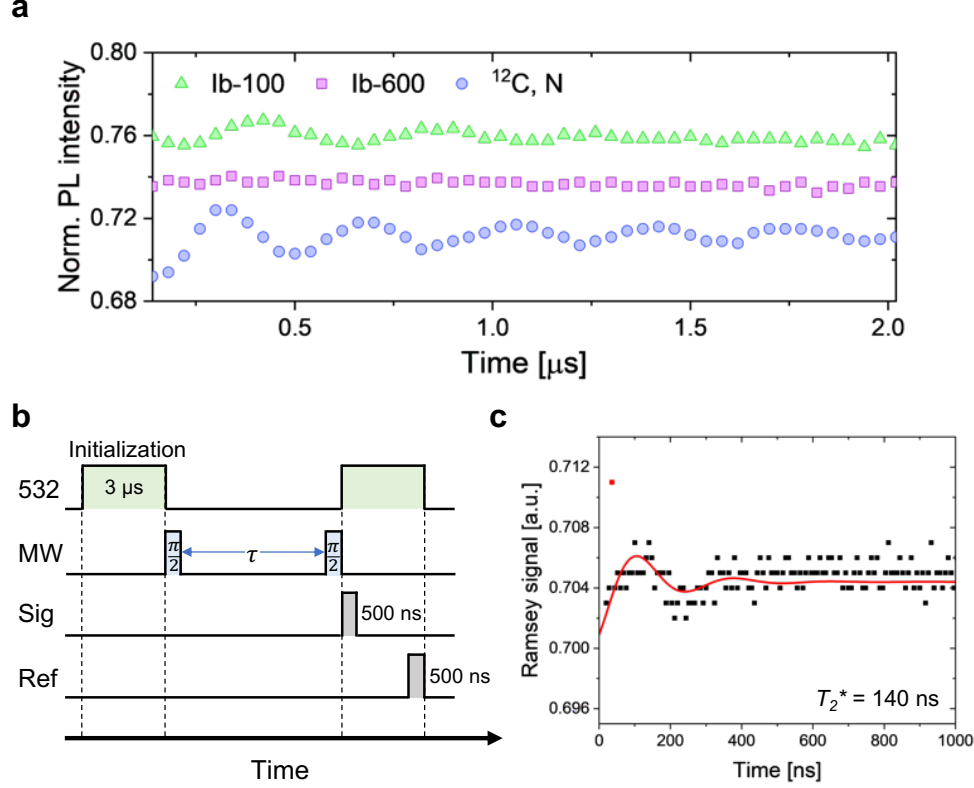


FIG. S10. (a) Comparison of Rabi oscillations between the different types of NDs at the same microwave power. Green triangle: Ib-100, purple square: Ib-600, blue circle: ^{12}C , N-NDs. In these measurements, we accumulated the data 20 times with the same measurement time step. (b) Schematic sequences of the Ramsey measurement. (c) Ramsey oscillation of a ^{12}C , N-ND, where the data was accumulated 20 times. The observed signal (plot data) is fitted using the sine-damping equation (red line). A red point contained one-time noise spike and excluded from the fitting.

- [1] G. Kucsko, P. C. Maurer, N. Y. Yao, M. Kubo, H. J. Noh, P. K. Lo, H. Park, and M. D. Lukin, “Nanometre-scale thermometry in a living cell,” *Nature* **500**, 54–58 (2013).
- [2] B. S. Miller, L. Bezing, H. D. Gliddon, D. Huang, G. Dold, E. R. Gray, J. Heaney, P. J. Dobson, E. Nastouli, J. J. L. Morton, and R. A. McKendry, “Spin-enhanced nanodiamond biosensing for ultrasensitive diagnostics,” *Nature* **587**, 588–593 (2020).
- [3] R. Geng, A. Mena, W. J. Pappas, and D. R. McCamey, “Sub-micron spin-based magnetic field imaging with an organic light emitting diode,” *Nat. Commun.* **14**, 1441 (2023).
- [4] S. Liu, A. Fossati, D. Serrano, A. Tallaire, A. Ferrier, and P. Goldner, “Defect engineering for quantum grade rare-earth nanocrystals,” *ACS Nano* **14**, 9953–9962 (2020).
- [5] N. Ronceray, Y. You, E. Glushkov, M. Lihter, B. Rehl, T. H. Chen, G. H. Nam, F. Borza, K. Watanabe, T. Taniguchi, S. Roke, A. Keerthi, J. Comtet, B. Radha, and A. Radenovic, “Liquid-activated quantum emission from pristine hexagonal boron nitride for nanofluidic sensing,” *Nat. Mater.* **22**, 1236–1242 (2023).
- [6] I. Aharonovich, J. P. Tetienne, and M. Toth, “Quantum emitters in hexagonal boron nitride,” *Nano Lett.* **22**, 9227–9235 (2022).
- [7] N. Aslam, H. Zhou, E. K. Urbach, M. J. Turner, R. L. Walsworth, M. D. Lukin, and H. Park, “Quantum sensors for biomedical applications,” *Nat. Rev. Phys.* **5**, 157–169 (2023).

- [8] H. Knowles and J. W. Hart, “Multimodal quantum metrology in living systems using nitrogen-vacancy centres in diamond nanocrystals,” *Front. Quantum Sci. Technol.* **2**, 1220015.
- [9] S. Haziza, N. Mohan, Y. Loe-Mie, A. M. Lepagnol-Bestel, S. Massou, M. P. Adam, X. L. Le, J. Viard, C. Plancon, R. Daudin, P. Koebel, E. Dorard, C. Rose, F. J. Hsieh, C. C. Wu, B. Potier, Y. Herault, C. Sala, A. Corvin, B. Allinquant, H. C. Chang, F. Treussart, and M. Simonneau, “Fluorescent nanodiamond tracking reveals intraneuronal transport abnormalities induced by brain-disease-related genetic risk factors,” *Nat. Nanotechnol.* **12**, 322–328 (2017).
- [10] N. Komatsu, “Poly (glycerol)-based biomedical nanodevices constructed by functional programming on inorganic nanoparticles for cancer nanomedicine,” *Acc. Chem. Res.* **56**, 106–116 (2023).
- [11] V. Vijayanthimala, P. Y. Cheng, S. H. Yeh, K. K. Liu, C. H. Hsiao, J. I. Chao, and H. C. Chang, “The long-term stability and biocompatibility of fluorescent nanodiamond as an in vivo contrast agent,” *Biomaterials* **33**, 7794–7802 (2012).
- [12] M. W. Doherty, N. B. Manson, P. Delaney, F. Jelezko, J. Wrachtrup, and L. C. L. Hollenberg, “The nitrogen-vacancy colour centre in diamond,” *Phys. Rep.* **528**, 1–45 (2013).
- [13] T. Fujisaku, R. Tanabe, S. Onoda, R. Kubota, T. F. Segawa, F. T. K. So, T. Ohshima, I. Hamachi, M. Shirakawa, and R. Igarashi, “pH nanosensor using electronic spins in diamond,” *ACS Nano* **13**, 11726–11732 (2019).
- [14] M. Sow, H. Steuer, S. Adekanye, L. Ginés, S. Mandal, B. Gilboa, O. A. Williams, J. M. Smith, and A. N. Kapanidis, “High-throughput nitrogen-vacancy center imaging for nanodiamond photophysical characterization and pH nanosensing,” *Nanoscale* **12**, 21821–21831 (2020).
- [15] S. Steinert, F. Ziem, L. T. Hall, A. Zappe, M. Schweikert, N. Götz, A. Aird, G. Balasubramanian, L. Hollenberg, and J. Wrachtrup, “Magnetic spin imaging under ambient conditions with sub-cellular resolution,” *Nat. Commun.* **4**, 1607 (2013).
- [16] F. A. Freire-Moschovitis, R. Rizzato, A. Pershin, M. R. Schepp, R. D. Allert, L. M. Todenhagen, M. S. Brandt, A. Gali, and D. B. Bucher, “The role of electrolytes in the relaxation of near-surface spin defects in diamond,” *ACS Nano* **17**, 10474–10485 (2023).
- [17] L. Nie, A. C. Nusantara, V. G. Damle, R. Sharmin, E. P. P. Evans, S. R. Hemelaar, K. J. Van der Laan, R. Li, F. P. Perona Martinez, T. Vedelaar, M. Chipaux, and R. Schirhagl, “Quantum monitoring of cellular metabolic activities in single mitochondria,” *Sci. Adv.* **7**, eabf0573 (2021).
- [18] A. Sigaeva, H. Shirzad, F. P. Martinez, A. C. Nusantara, N. Mougios, M. Chipaux, and R. Schirhagl, “Diamond-based nanoscale quantum relaxometry for sensing free radical production in cells,” *Small* **18**, 2105750 (2022).
- [19] X. Feng, W. H. Leong, K. Xia, C. F. Liu, G. Q. Liu, T. Rendler, J. Wrachtrup, R. B. Liu, and Q. Li, “Association of nanodiamond rotation dynamics with cell activities by translation-rotation tracking,” *Nano Lett.* **21**, 3393–3400 (2021).
- [20] Q. Gu, L. Shanahan, J. W. Hart, S. Belser, N. Shofer, M. Atature, and H. S. Knowles, “Simultaneous nanorheometry and nanothermometry using intracellular diamond quantum sensors,” *ACS Nano* **17**, 20034–20042 (2023).
- [21] J. F. Barry, J. M. Schloss, E. Bauch, M. J. Turner, C. A. Hart, L. Pham, and R. L. Walsworth, “Sensitivity optimization for NV-diamond magnetometry,” *Rev. Mod. Phys.* **92**, 015004 (2020).
- [22] C. L. Degen, F. Reinhard, and P. Cappellaro, “Quantum sensing,” *Rev. Mod. Phys.* **89**, 035002 (2017).
- [23] N. Mizuochi, P. Neumann, F. Rempp, J. Beck, V. Jacques, P. Siyushev, K. Nakamura, D. J. Twitchen, H. Watanabe, S. Yamasaki, F. Jelezko, and J. Wrachtrup, “Coherence of single spins coupled to a nuclear spin bath of varying density,” *Phys. Rev. B* **80**, 041201 (2009).
- [24] H. S. Knowles, D. M. Kara, and M. Atatüre, “Observing bulk diamond spin coherence in high-purity nanodiamonds,” *Nat. Mater.* **13**, 21–25 (2014).
- [25] Y. Romach, C. Müller, T. Unden, L. J. Rogers, T. Isoda, K. M. Itoh, M. Markham, A. Stacey, J. Meijer, S. Pezzagna, B. Naydenov, L. P. McGuinness, N. Bar-Gill, and F. Jelezko, “Spectroscopy of surface-induced noise using shallow spins in diamond,” *Phys. Rev. Lett.* **114**, 017601 (2015).
- [26] P. Andrich, B. J. Alemán, J. C. Lee, K. Ohno, C. F. de las Casas, F. J. Heremans, E. L. Hu, and D. D. Awschalom, “Engineered micro- and nanoscale diamonds as mobile probes for high-resolution sensing in fluid,” *Nano Lett.* **14**, 4959–4964 (2014).
- [27] E. D. Herbschleb, H. Kato, Y. Maruyama, T. Danjo, T. Makino, S. Yamasaki, I. Ohki, K. Hayashi, H. Morishita, M. Fujiwara, and N. Mizuochi, “Ultra-long coherence times amongst room-temperature solid-state spins,” *Nat. Commun.* **10**, 3766 (2019).
- [28] E. Bauch, S. Singh, J. Lee, C. A. Hart, J. M. Schloss, M. J. Turner, J. F. Barry, L. M. Pham, N. Bar-Gill, S. F. Yelin, and R. L. Walsworth, “Decoherence of ensembles of nitrogen-vacancy centers in diamond,” *Phys. Rev. B* **102**, 134210 (2020).
- [29] C. Shinei, M. Miyakawa, S. Ishii, S. Saiki, S. Onoda, T. Taniguchi, T. Ohshima, and T. Teraji, “Equilibrium charge state of NV centers in diamond,” *Appl. Phys. Lett.* **119**, 254001 (2021).
- [30] T. Wolf, P. Neumann, K. Nakamura, H. Sumiya, T. Ohshima, J. Isoya, and J. Wrachtrup, “Subpicotesla diamond magnetometry,” *Phys. Rev. X* **5**, 041001 (2015).
- [31] M. H. Aboeib, J. Randall, C. E. Bradley, H. P. Bartling, M. A. Bakker, M. J. Degen, M. Markham, D. J. Twitchen, and T. H. Taminiau, “Atomic-scale imaging of a 27-nuclear-spin cluster using a quantum sensor,” *Nature* **576**, 411–415 (2019).
- [32] C. Zhang, J. Zhang, M. Widmann, M. Benke, M. Kübler, D. Dasari, T. Klotz, L. Gizzi, O. Röhrle, P. Brenner, and J. Wrachtrup, “Optimizing NV magnetometry for magnetoneurography and magnetomyography applications,” *Front. Neurosci.* **16**, 1034391 (2023).
- [33] J. P. Tetienne, T. Hingant, L. Rondin, A. Cavallès, L. Mayer, G. Dantelle, T. Gacoin, J. Wrachtrup, J. F. Roch, and V. Jacques, “Spin relaxometry of single nitrogen-vacancy defects in diamond nanocrystals for magnetic noise sensing,” *Phys. Rev. B* **87**, 235436 (2013).

- [34] M. Fujiwara, S. Sun, A. Dohms, Y. Nishimura, K. Suto, Y. Takezawa, K. Oshimi, L. Zhao, N. Sadzak, Y. Umehara, Y. Teki, N. Komatsu, O. Benson, Y. Shikano, and E. Kage-Nakadai, “Real-time nanodiamond thermometry probing in vivo thermogenic responses,” *Sci. Adv.* **6**, eaba9636 (2020).
- [35] J. E. March, B. D. Wood, C. J. Stephen, L. D. Ferverza, B. G. Breeze, S. Mandal, A. M. Edmonds, D. J. Twitchen, M. L. Markham, O. A. Williams, and G. W. Morley, “Long spin coherence and relaxation times in nanodiamonds milled from polycrystalline 12 C diamond,” *Phys. Rev. Appl.* **20**, 044045 (2023).
- [36] U. Zvi, D. R. Candido, A. Weiss, A. R. Jones, L. Chen, I. Golovina, X. Yu, S. Wang, D. V. Talapin, M. E. Flatté, A. P. Esser-Kahn, and P. C. Maurer, “Engineering spin coherence in core-shell diamond nanocrystals,” arXiv:2305.03075 (2023).
- [37] S. Eldemrdash, G. Thalassinou, A. Alzahrani, Q. Sun, E. Walsh, E. Grant, H. Abe, T. L. Greaves, T. Ohshima, P. Cigler, P. Matějček, D. A. Simpson, A. D. Greentree, G. Bryant, B. C. Gibson, and P. Reineck, “Fluorescent HPHT nanodiamonds have disk-and rod-like shapes,” *Carbon* **206**, 268–276 (2023).
- [38] K. Oshimi, Y. Nishimura, T. Matsubara, M. Tanaka, E. Shikoh, L. Zhao, Y. Zou, N. Komatsu, Y. Ikado, Y. Takezawa, E. Kage-Nakadai, Y. Izutsu, K. Yoshizato, S. Morita, M. Tokunaga, H. Yukawa, Y. Baba, Y. Teki, and M. Fujiwara, “Glass-patternable notch-shaped microwave architecture for on-chip spin detection in biological samples,” *Lab Chip* **22**, 2519–2530 (2022).
- [39] A. Jarmola, V. M. Acosta, K. Jensen, S. Chemerisov, and D. Budker, “Temperature-and magnetic-field-dependent longitudinal spin relaxation in nitrogen-vacancy ensembles in diamond,” *Phys. Rev. Lett.* **108**, 197601 (2012).
- [40] D. Maclaurin, L. T. Hall, A. M. Martin, and L. C. L. Hollenberg, “Nanoscale magnetometry through quantum control of nitrogen–vacancy centres in rotationally diffusing nanodiamonds,” *New J. Phys.* **15**, 013041 (2013).
- [41] M. Kayci, H. C. Chang, and A. Radenovic, “Electron spin resonance of nitrogen-vacancy defects embedded in single nanodiamonds in an ABEL trap,” *Nano Lett.* **14**, 5335–5341 (2014).
- [42] J. P. Tetienne, R. W. De Gille, D. A. Broadway, T. Teraji, S. E. Lillie, J. M. McCoe, N. Donschuk, L. T. Hall, A. Stacey, D. A. Simpson, and L. C. L. Hollenberg, “Spin properties of dense near-surface ensembles of nitrogen-vacancy centers in diamond,” *Phys. Rev. B* **97**, 085402 (2018).
- [43] H. S. Knowles, D. M. Kara, and M. Atatüre, “Demonstration of a coherent electronic spin cluster in diamond,” *Phys. Rev. Lett.* **117**, 100802 (2016).
- [44] L. M. Pham, N. Bar-Gill, C. Belthangady, D. Le Sage, P. Cappellaro, M. D. Lukin, A. Yacoby, and R. L. Walsworth, “Enhanced solid-state multispin metrology using dynamical decoupling,” *Phys. Rev. B* **86**, 045214 (2012).
- [45] M. Capelli, A. H. Heffernan, T. Ohshima, H. Abe, J. Jeske, A. Hope, A. D. Greentree, P. Reineck, and B. C. Gibson, “Increased nitrogen-vacancy centre creation yield in diamond through electron beam irradiation at high temperature,” *Carbon* **143**, 714–719 (2019).
- [46] T. Rosskopf, A. Dussaux, K. Ohashi, M. Loretz, R. Schirhagl, H. Watanabe, S. Shikata, K. M. Itoh, and C. L. Degen, “Investigation of surface magnetic noise by shallow spins in diamond,” *Phys. Rev. Lett.* **112**, 147602 (2014).
- [47] W. Zheng, K. Bian, X. Chen, Y. Shen, S. Zhang, R. Stöhr, A. Denisenko, J. Wrachtrup, S. Yang, and Y. Jiang, “Coherence enhancement of solid-state qubits by local manipulation of the electron spin bath,” *Nat. Phys.* **18**, 1317–1323 (2022).
- [48] G. Q. Liu, X. Feng, N. Wang, Q. Li, and R. B. Liu, “Coherent quantum control of nitrogen-vacancy center spins near 1000 kelvin,” *Nat. Commun.* **10**, 1344 (2019).
- [49] P. Konzelmann, T. Rendler, V. Bergholm, A. Zappe, V. Pfannenstill, M. Garsi, F. Ziem, M. Niethammer, M. Widmann, S. Y. Lee, P. Neumann, and J. Wrachtrup, “Robust and efficient quantum optimal control of spin probes in a complex (biological) environment. Towards sensing of fast temperature fluctuations,” *New J. Phys.* **20**, 123013 (2018).
- [50] I. Schwartz, J. Scheuer, B. Tratzmiller, S. Müller, Q. Chen, I. Dhand, Z. Y. Wang, C. Müller, B. Naydenov, F. Jelezko, and M. B. Plenio, “Robust optical polarization of nuclear spin baths using hamiltonian engineering of nitrogen-vacancy center quantum dynamics,” *Sci. Adv.* **4**, eaat8978 (2018).
- [51] K. Ikeda and H. Sumiya, “Optical properties of ultrapure nano-polycrystalline diamond,” *Jpn. J. Appl. Phys.* **55**, 120306 (2016).
- [52] H. Deguchi, T. Hayashi, H. Saito, Y. Nishibayashi, M. Teramoto, M. Fujiwara, H. Morishita, N. Mizuochi, and N. Tatsumi, “Compact and portable quantum sensor module using diamond NV centers,” *Appl. Phys. Express* **16**, 062004 (2023).
- [53] J. Canet-Ferrer, E. Coronado, A. Forment-Aliaga, and E. Pinilla-Cienfuegos, “Correction of the tip convolution effects in the imaging of nanostructures studied through scanning force microscopy,” *Nanotechnology* **25**, 395703 (2014).
- [54] S. Stehlik, M. Varga, M. Ledinsky, V. Jirasek, A. Artemenko, H. Kozak, L. Ondic, V. Skakalova, G. Argentero, T. Pennycook, J. C. Meyer, A. Fejfar, A. Kromka, and B. Rezek, “Size and purity control of hpht nanodiamonds down to 1 nm,” *J. Phys. Chem. C* **119**, 27708–27720 (2015).
- [55] R. Tsukahara, M. Fujiwara, Y. Sera, Y. Nishimura, Y. Sugai, C. Jentgens, Y. Teki, H. Hashimoto, and S. Shikata, “Removing non-size-dependent electron spin decoherence of nanodiamond quantum sensors by aerobic oxidation,” *ACS Appl. Nano Mater.* **2**, 3701–3710 (2019).
- [56] M. Fujiwara, A. Dohms, K. Suto, Y. Nishimura, K. Oshimi, Y. Teki, K. Cai, O. Benson, and Y. Shikano, “Real-time estimation of the optically detected magnetic resonance shift in diamond quantum thermometry toward biological applications,” *Phys. Rev. Res.* **2**, 043415 (2020).
- [57] A. Dréau, M. Lesik, L. Rondin, P. Spinicelli, O. Arcizet, J. F. Roch, and V. Jacques, “Avoiding power broadening in optically detected magnetic resonance of single nv defects for enhanced dc magnetic field sensitivity,” *Phys. Rev. B* **84**, 195204 (2011).
- [58] P. Ferrand, “GPScan. VI: A general-purpose labview program for scanning imaging or any application requiring synchronous analog voltage generation and data acquisition,” *Comput. Phys. Commun.* **192**, 342–347 (2015).

- [59] S. T. Alsid, J. F. Barry, L. M. Pham, J. M. Schloss, M. F. O’Keeffe, P. Cappellaro, and D. A. Braje, “Photoluminescence decomposition analysis: A technique to characterize N-V creation in diamond,” *Phys. Rev. Appl.* **12**, 044003 (2019).
- [60] J. Teissier, A. Barfuss, P. Appel, E. Neu, and P. Maletinsky, “Strain coupling of a nitrogen-vacancy center spin to a diamond mechanical oscillator,” *Phys. Rev. Lett.* **113**, 020503 (2014).
- [61] M. W. Doherty, V. V. Struzhkin, D. A. Simpson, L. P. McGuinness, Y. Meng, A. Stacey, T. J. Karle, R. J. Hemley, N. B. Manson, L. C. L. Hollenberg, and S. Praver, “Electronic properties and metrology applications of the diamond NV⁻ center under pressure,” *Phys. Rev. Lett.* **112**, 047601 (2014).
- [62] S. Sotoma, D. Terada, T. F. Segawa, R. Igarashi, Y. Harada, and M. Shirakawa, “Enrichment of odmr-active nitrogen-vacancy centres in five-nanometre-sized detonation-synthesized nanodiamonds: Nanoprobes for temperature, angle and position,” *Sci. Rep.* **8**, 5463 (2018).
- [63] L. Robledo, H. Bernien, T. Van Der Sar, and R. Hanson, “Spin dynamics in the optical cycle of single nitrogen-vacancy centres in diamond,” *New J. Phys.* **13**, 025013 (2011).
- [64] F. C. Ziem, N. S. Götz, A. Zappe, S. Steinert, and J. Wrachtrup, “Highly sensitive detection of physiological spins in a microfluidic device,” *Nano Lett.* **13**, 4093–4098 (2013).
- [65] F. Perona Martínez, A. C. Nusantara, M. Chipaux, S. K. Padamati, and R. Schirhagl, “Nanodiamond relaxometry-based detection of free-radical species when produced in chemical reactions in biologically relevant conditions,” *ACS Sens.* **5**, 3862–3869 (2020).
- [66] I. C. Barbosa, J. Gutsche, and A. Widera, “Impact of charge conversion on NV-center relaxometry,” *Phys. Rev. B* **108**, 075411 (2023).
- [67] I. C. Barbosa, J. Gutsche, D. Lönard, S. Dix, and A. Widera, “Temperature dependence of charge conversion during NV-center relaxometry,” *arXiv:2309.12131* (2023).
- [68] Y. Nishimura, K. Oshimi, Y. Umehara, Y. Kumon, K. Miyaji, H. Yukawa, Y. Shikano, T. Matsubara, M. Fujiwara, Y. Baba, and Y. Teki, “Wide-field fluorescent nanodiamond spin measurements toward real-time large-area intracellular thermometry,” *Sci. Rep.* **11**, 4248 (2021).
- [69] H. Yukawa, M. Fujiwara, K. Kobayashi, Y. Kumon, K. Miyaji, Y. Nishimura, K. Oshimi, Y. Umehara, Y. Teki, T. Iwasaki, M. Hatano, H. Hashimoto, and Y. Baba, “A quantum thermometric sensing and analysis system using fluorescent nanodiamonds for the evaluation of living stem cell functions according to intracellular temperature,” *Nanoscale Adv.* **2**, 1859–1868 (2020).
- [70] N. Chertkova and S. Yamashita, “In situ spectroscopic study of water speciation in the depolymerized Na₂Si₂O₅ melt,” *Chem. Geol.* **409**, 149–156 (2015).
- [71] T. Sano and S. Yamashita, “Evolution, hydrothermal assimilation, and ascent of magma inferred from volatile contents in MORB glasses: An example from thick lava pile at IODP Site 1256,” *Lithos* **346**, 105143 (2019).
- [72] Z. Z. Liang, X. Jia, H. A. Ma, C. Y. Zang, P. W. Zhu, Q. F. Guan, and H. Kanda, “Synthesis of HPHT diamond containing high concentrations of nitrogen impurities using NaN₃ as dopant in metal-carbon system,” *Diam. Relat. Mater.* **14**, 1932–1935 (2005).
- [73] A. Kuwahata, T. Kitaizumi, K. Saichi, T. Sato, R. Igarashi, T. Ohshima, Y. Masuyama, T. Iwasaki, M. Hatano, F. Jelezko, M. Kusakabe, T. Yatsui, and M. Sekino, “Magnetometer with nitrogen-vacancy center in a bulk diamond for detecting magnetic nanoparticles in biomedical applications,” *Sci. Rep.* **10**, 2483 (2020).
- [74] G. J. Abrahams, E. Ellul, I. O. Robertson, A. Khalid, A. D. Greentree, B. C. Gibson, and J. P. Tetienne, “Handheld device for noncontact thermometry via optically detected magnetic resonance of proximate diamond sensors,” *Phys. Rev. Appl.* **19**, 054076 (2023).
- [75] M. Fujiwara, Y. Shikano, R. Tsukahara, S. Shikata, and H. Hashimoto, “Observation of the linewidth broadening of single spins in diamond nanoparticles in aqueous fluid and its relation to the rotational brownian motion,” *Sci. Rep.* **8**, 14773 (2018).
- [76] T. Teraji and C. Shinei, “Nitrogen-related point defects in homoepitaxial diamond (001) freestanding single crystals,” *J. Appl. Phys.* **133**, 165101 (2023).